Title

Direct Imaging of Grain Boundaries

Author

Gronsky, R

Publication Date

1979-09-01

Lawrence Berkeley Laboratory

UNIVERSITY OF CALIFORNIA

Materials & Molecular Research Division

Presented at the ASM Science Seminar, Milwaukee, WI, September 15-16, 1979

DIRECT IMAGING OF GRAIN BOUNDARIES

R. Gronsky

September 1979

Prepared for the U.S. Department of Energy under Contract W-7405-ENG-48

DISCLAIMER

DIRECT IMAGING OF GRAIN BOUNDARIES

R. Gronsky

Materials and Molecular Research Division
Lawrence Berkeley Laboratory, Berkeley, CA 94720

ABSTRACT

There are currently two types of microscopes which, in principle, are capable of imaging atom positions at grain boundaries. One, the field ion microscope (FIM), yields a projection of the specimen surface (approximately stereographic) by field ionization of an imaging gas at protruding atom sites, and provides topographic information in high-index pole regions which may be interpreted atom-by-atom. The other, a transmission electron microscope (TEM), yields a projection (approximately linear) of the entire specimen thickness by electron optical imaging, and provides atomic resolution detail throughout the illuminated area. In this paper, both methods are described and compared, using examples from practical materials systems.

I. INTRODUCTION

Materials scientists have long been aware that there is much to be learned about the behavior of grain boundaries from a detailed understanding of their structure. Problems such as intergranular embrittlement, intergranular corrosion, segregation, recrystallization texture, and boundary migration rates are all intimately connected to the nature of atomic bonding across a grain boundary.[1] Some success in describing these phenomena has been realized by theoretical models of boundary structure which are based upon the concept of a transition lattice;[2] but the shortcomings of these models are most obvious in those regions of the crystal where they are most needed: a monolayer or two on either side of the boundary plane.

The study of grain boundaries is therefore best accomplished by experimental methods which provide a *direct* image of local atomic arrangements across the boundary vicinity. While it is true that some of this information may be obtained by indirect methods, i.e. diffraction,[3] there are still considerable problems in interpretation, particularly of the ambiguities present in diffuse scattering from non-periodic defects.

In this context, the present paper presents a review of currently available techniques for direct imaging of grain boundaries: field ion microscopy and transmission electron microscopy. Details of operation, image formation, image interpretation and applications to the study of boundaries are described and compared. Although the complementary capabilities of both types of instrument for chemical microanalysis are

equally impressive,[4,5] such topics are beyond the scope of the present article. Emphasis is instead placed on the advantages and limitations of these techniques, both obvious and subtle, for high resolution structural analysis, including recent progress in the development of atomic resolution microscopy.

II. FIELD ION MICROSCOPY

II.1 Principles

Erwin Müller's development of the field emission microscope (FEM) led promptly to the field ion microscope (FIM), principally as a result of his search for increased resolution.[6] Due to the lateral velocity component of its emitted electrons, the FEM is restricted to $\simeq 25\text{Å}$ resolution, whereas the FIM can achieve an order of magnitude better, thereby making it a candidate for imaging atomic structure. The essential features of the two instruments are the same: a pointed emitter tip which is fabricated from the specimen material, an applied potential to produce and accelerate the imaging particles, an evacuated column, and an image intensifier/recording system, usually based on a fluorescent screen. Details of typical systems are available in several good reviews.[7,8]

In the FIM, the imaging particles are gas ions, obtained by bleeding neutral gas molecules at low pressure ($\simeq 10^{-3}$ torr) into the specimen chamber. These molecules are preferentially ionized at the locations of highest electric field surrounding the positively-charged emitter tip and subsequently accelerated from these ionization sites to the imaging screen, which is held at ground potential. It is emphasized that the field ion image is actually a mapping of the electric field distribution a small distance above the emitter tip;[9] this fact has important implications in image interpretation as explained in the next section. Note also that there are no focusing lenses in the FIM, making it more of a projection device than a "microscope." However, the projection process

results in appreciable magnification ($\simeq 10^7$X), enabling the individual ionization sites to be distinguished.

II.2 Image Formation and Interpretation

The FIM image, therefore, exhibits the arrangement of gas ionization sites very near the specimen surface. Obviously, if the atomic structure of the specimen is to be resolved by this technique, then each ionization site must be separated by a single interatomic spacing. Reference to the first figure shows that this condition is sometimes, but not always, realized.

Figure 1 depicts the geometry, in rough schematic form, of a typical FIM emitter tip. Although the overall shape of the tip is smooth, there can be severe distortions in local radius, depending upon local atomic structure. These in turn affect the local field distribution, such that the electric field is highest at surface atom protrusions. Note from Fig. 1 that such sites (S) which mark the sites at which gas molecules will be preferentially ionized, are widely spaced in the low-index pole regions (e.g., L) of the tip, but become much more closely spaced in the high-index pole regions (e.g., H). Based solely upon tip geometry, then, resolution of atomic structure will only occur where the specimen surface is parallel to the high-index planes of the atomic lattice, or where the low-index plane surfaces are very small in area.[10] Isolated atoms which by chance protrude from larger segments of low-index plane surfaces will also be observed, but their structural relationship to contiguous atoms will not be obvious.

Another geometrical aspect of the imaging process which affects interpretation and resolution is the nature of the projection itself. The dashed line in Fig. 2 represents a reasonably probable trajectory[7] of an ion in going from the surface of the emitter tip at X to the imaging screen at X'; the exact trajectory path has not yet been established.[11] The extrapolation of all possible lines X'X back through their intersection with the centerline axis of the emitter tip define a projection point P, located at distance Nr behind the spherical surface (radius r) of the emitter tip. Also plotted at the screen position are the points at which X would appear in standard gnomonic (G), stereographic (S), and orthographic (O) projections, for which N = 0, 1 and ∞, respectively. An alternative, non-standard projection suggested by Brandon,[12] which sets N equal to 2, is also plotted (B). Note that in general, none of these projections give an exact fit to the typical FIM image. It has recently been shown[11] however, that most FIM micrographs can be proportionally scaled to a stereographic projection via a constant factor. For analysis of atomic arrangements at structural discontinuities, this factor must be determined with high precision.

Figure 3 demonstrates the interpretation of a field ion micrograph in terms of a standard stereographic projection. The micrograph in (a) is a particularly striking example, taken from a fully ordered Ni_4W specimen.[13] It is apparent that the overall symmetry of the b.c.t. stereographic projection in (b) occurs in the image; however, atomic

level discrepancies are readily found by closer scrutiny of the image spot patterns. These are common to all FIM images and represent an increase in magnification for poles inclined at large angles to the tip axis.[8]

Other more severe effects which prevent atomic resolution in the FIM stem from the spatial distortions in the emitter tip induced by the high applied field. These stresses may modify the atomic arrangement being studied, such that the actual structure is grossly misrepresented. Frequent causes are: a non-uniform distribution in the applied field,[14] elastic anisotropy of the specimen,[14] preferential field evaporation of atoms at the core of defects,[15] and polarization bonding[16] which results in "zone decoration." Less severe, but equally damaging to resolution, are image instabilities produced when surface atoms are brought to their evaporation threshold by the local field. Often such effects can only be identified by comparisons with computed images (cf. Fig. 4).

II.3 Applications to Grain Boundaries

Each of these limitations, of course, becomes all the more pronounced when applied to the imaging of atomic structure at grain boundaries. Recognizing that the most significant result to be obtained from such an experiment is the nature of bonding *across* the boundary plane, the constraints imposed by the geometry of the specimen are illustrated in Fig. 5. This schematic FIM image of a grain boundary demonstrates that contrast at a boundary is produced by the mismatch of the characteristic

In another study,[20] oxygen segregation to tungsten grain boundaries was imaged at monolayer thickness (see Fig. 9); however, resolution was again insufficient to determine the exact nature of the solute sites.

III. TRANSMISSION ELECTRON MICROSCOPY

III.1 Principles

Unlike the FIM, a transmission electron microscope (TEM) is accurately classified as an electron optical device and its operating principles are firmly established in traditional theories of optics. The instrument consists of an electron gun illumination source, a series of electromagnetic lenses, a stage for manipulation of the specimen under the beam, and an image display/recording system, all housed in an evacuated column. The TEM is generally in more widespread use than the FIM and its applications in materials science have been described in numerous reviews.[21-23]

Because it operates in a transmission mode, the TEM requires specimens which have been thinned to electron transparency. The electrons which traverse the foil are brought to focus by an objective lens that is coupled to a projection system for display on a fluorescent screen at up to 10^6X enlargement. Atomic resolution images obtained in this way are therefore a projection of atomic columns through the thickness of the foil. In addition, there are no inherent mechanisms in the image formation process which physically prevent seeing the structural arrangement of neighboring atoms in the projection plane. This is a consequence of any optical system: each object point (atom columns) can potentially be mapped, simultaneously, as an image point with sufficiently precise experimental control. The required extent of this control is outlined in the following section.

III.2 Image Formation and Interpretation

Conventional image fomration in the TEM is achieved by magnifying either the forward-scattered beam, to form a bright field image, or one of the Bragg-scattered beams, to form a dark field image. The mechanisms responsible for contrast under these conditions have been understood and utilized for quite some time.(21) Nevertheless, single beam imaging cannot reveal the atomic structure of the specimen due to its highly restricted sampling of reciprocal space. Figure 10 schematically illustrates the nature of this problem.

According to Abbé's theory(24) the complete diffraction pattern appearing at the back focal plane of the objective lens is actually a mapping of the Fourier transform of the specimen. Maximum information about the specimen, i.e., at highest resolution, should therefore be obtained by an inverse Fourier transform where all Fourier coefficients have been retained. This is realized in practice by including *all* beams from the diffraction pattern in the imaging aperture. Unfortunately, this process is only possible for a perfect objective lens of infinite aperture. Real electron optical systems introduce modifications in both amplitude, due to a finite aperture size, and phase, due to lens aberrations, of the intensity distribution at the back focal plane.(25)

The phase distortion of a beam located at $\underset{\sim}{q}$ from the optic axis is described(26) by a function

$$X(\underset{\sim}{q}) = \frac{2\pi}{\lambda}\left(C_s \frac{\lambda^4 q^4}{4} + \Delta z \frac{\lambda^2 q^2}{2}\right) \qquad (1)$$

where C_s is the spherical aberration coefficient and Δz the extent of defocus of the objective for an electron wavelength λ. Note that at underfocus (negative Δz) the detrimental effects of spherical aberration can be partially compensated.[27] In general, however, the spatial information contained within a particular beam at $\underset{\sim}{q}_1$ will be faithfully transferred to the image only when its corresponding phase factor $\exp(i\ X(\underset{\sim}{q}_1))$ is near unity. For this reason, the variation of $\exp(i\ X(\underset{\sim}{q}))$ over all reciprocal space, known as the contrast transfer function (CTF), gives an indication of the imaging capabilities of an objective lens. As shown in Fig. 10, the diffraction spectra are modified by the CTF before inverse transformation to the image plane. Obviously, the exact relationship between image detail and object detail is also contained in the transfer function.

It is instructive to examine the behavior of the CTF with changes in focus, since this is usually the only parametric control left to the operator of a given TEM. One example is presented in Fig. 11, computed on the basis of Equation 1, and showing the variation $2 \sin X(\underset{\sim}{q})$ vs. $\underset{\sim}{q}$ for 100kV electrons and C_s = 0.7 mm. The corresponding defocus values are: (a) 0, (b) -600, (c) -1200 and (d) -1400 Å. It is obvious from this figure that, contrary to intuition, there is actually less resolution in a "perfectly focused" micrograph ($\Delta z = 0$) than in one which is taken "out of focus." This conclusion stems from the maximum value of the transfer function at the higher spatial frequency values (large $\underset{\sim}{q}$), where resolution is greatest, in (b), (c), and (d). Note in (b) the emergence

of a broad transfer interval, representing a relatively large region of reciprocal space over which object detail is preserved in the image. This main transfer interval then moves to even higher $\underset{\sim}{q}$ with increasingly larger underfocus. By comparison, an image taken at exact focus is limited to ≈5Å point-to-point resolution ($\underset{\sim}{q}_{max.} \simeq .25$ in (a)) while at -1200Å underfocus, resolution is improved to ≈ 2.5Å point-to-point ($\underset{\sim}{q}_{max.} \simeq .4$ in (b)). From this setting, a further change in focus of only 200Å (cf. Fig. 11(d)) reverses image contrast, i.e. atoms appearing as white dots above a black background become black dots on a white background.

An experimental determination of the transfer function would be a useful aid in image interpretation. This can be accomplished by imaging in the TEM a specimen which is representative of *all* possible spatial frequencies, e.g. an "amorphous" material. Using the negative TEM image as a diffraction grating, an optical diffraction pattern would then show which spatial frequencies were actually imaged,[28] and which were filtered out due to the local minima in the CTF, i.e., the "power spectrum." Figure 12 is an example of such an experiment. In going from "exact focus" in (a), to 800Å underfocus in (b), to 2200Å underfocus in (c), the outward motion of the main transfer interval is apparent. Note that as the main interval, depicted by the diffuse halo, extends radially, the diffraction spots emanating from image detail increase in intensity, representing an increase in image contrast. Also in (c) a new set of higher order diffraction spots appear, representing an increase in

resolution. In this manner, an optimum imaging condition for atomic level detail can be readily determined.

Similar manipulations of the transfer function have resulted in spectacular TEM images of atomic structure. The example given in Fig. 13 is one such case[29] comparing the white dot images of atom columns in a [110] oriented silicon crystal with a schematic projection of the atomic positions in a [110] oriented diamond cubic lattice. The agreement is one-to-one at 1.4Å resolution.

III.3 Applications to Grain Boundaries

The difficulties involved in imaging atomic positions at grain boundaries become obvious when it is realized that this requires sufficient breadth in the main transfer interval to accommodate not only the Bragg peaks from a single perfect crystal, but the Bragg peaks from a second, misoriented, perfect crystal, *and* the diffuse scattering arising from the defect structure of the boundary as well. A typical experimental case might be as shown in Fig. 14. Here, the limit of effective contrast transfer has been set at the position of the dashed line. Note that although all of the low index planes from grain 1 will be imaged in this case, only one set of such planes from grain 2 will appear. Since atomic positions are delineated by the intersections of these planes, the atoms in only one grain will be seen, with the detailed structural configuration across the boundary necessarily lost in consequence.

There are other concerns in high resolution imaging of boundaries which derive purely from the choice of imaging reflections. These are

illustrated via a one-dimensional optical analog in Figs. 15 and 16.

The "specimen" chosen for this experiment is pictured by simple photogram in Fig. 15. It is an electron microscope support grid, 3 mm in diameter, with two distinct sets of grid spacings, half of them narrow and half wide, joined in the center. A small square at the center represents two-dimensional detail at the "boundary" plane, and there are obvious "point" defects, one in the wide grid region, one (smaller) in the narrow grid region. The actual grid (which is the "negative" of this image) was placed in an optical bench and imaged with laser illumination under the conditions shown in Fig. 16.

By full recombination of the entire diffraction pattern (Fig. 16(a)), all the detailed features of the object were accurately imaged. However, a more realistic representation of the limitations of an optical transfer function was produced by inserting a 1 mm diameter aperture at the back focal plane of the objective, truncating the higher order diffracted intensities. The result (Fig. 16(b)) is again a recognizable image in which the prominent features of the object have been retained. Note, however, that the central square is now circular due to the loss of the higher order harmonics in the Fourier spectrum, and that while the smaller point defect is gone, the larger one is still apparent.

Under even more restrictive imaging conditions, simulated by a 600 μm aperture at the back focal plane, the image of the boundary can be severely aberrated. Figure 16(c) demonstrates that by mistakenly choosing the diffracted intensities from the wide grid region only,

(e.g., a single grain), the image loses all evidence of a grain boundary. In fact, the wider grid spacings are reproduced across the entire image, even into the narrow grid region. It is therefore not surprising that the two-dimensional details are also unrecognizable.

Finally, Fig. 16(d) shows that even with the imposition of severe aperture restrictions, as in the case of a limited transfer interval, the characteristics of the boundary region can be salvaged. Here, the aperture was positioned so as to include a single reflection from each grain, representing a Fourier transformation in which only the first order coefficients have been retained. Note that in spite of the loss of two-dimensional detail, the "boundary" has indeed been properly imaged with the correct number of "lattice planes" on either side.

An experiment of this sort emphasises that there is much to be gained from direct imaging of boundaries using only two beams, which reveal the matching of lattice planes at the boundary region.[30] Two examples of this technique are presented in the following micrographs.

Figure 17 shows an image of the close-packed (111) planes in an aluminum-base alloy as they cross a small angle grain boundary. At this level of resolution, the accommodation of mismatch can be localized to within a single lattice plane (solid arrow); however, regions of extended accommodation are also visible (between open arrows). By imaging the lattice planes which parallel the boundary plane, (Fig. 18) microledge structures are clearly revealed (arrowed), even though they are only a single lattice plane spacing in height. The ledges are observed at a density

which establishes the macroscopic orientation changes in grain boundary facets.

Most metals and alloys are sufficiently close-packed so that even with the use of a high order transfer interval in a conventional TEM, resolution is limited to the lattice plane level as shown above. However, with specimens of a more open structure, the probability of achieving multi-dimensional lattice images, or structural images, is vastly improved. A large class of commercial materials based upon the diamond-cubic structure fall into this category, e.g., Si or Ge semiconductor devices.

By combining all first order reflections in a [110] zone, the structural image of a small angle grain boundary in Si, shown in Fig. 19, was obtained. The interesting aspect of this image is the crystallography of the large scale facets in the boundary plane, which follow the traces of all of the low index families. Detailed studies of the atomic matching across the boundary show that the regions of greatest disturbance are at the intersections of these ledges, and may represent extended core regions of the boundary dislocation net.

The same imaging condition applied to a higher angle boundary yielded the result in Fig. 20(a) for a Ge specimen.[31] A number of microtwins (arrowed) is seen in addition to the horizontally oriented grain boundary, which is characterized by an alternating array of larger and smaller white spots than those seen within the neighboring grains. The detailed model of the boundary, derived from this image and shown in Fig. 20(b), depicts

the atomic structure of the boundary as alternating seven-membered and five-membered rings of Ge atoms, while the surrounding matrix structure is six-membered. There is clearly no discrepancy in the nature of atomic arrangements across the boundary plane; no dangling bonds are observed, and the coincidence site lattice ($\Sigma = 9$, 39°<011>) can be precisely distinguished.

In more recent technological advances, the performance of higher voltage TEM's has been improved such that atomic resolution imaging of grain boundaries in even the most close-packed materials is now possible.[32] Figures 21 and 22 are examples taken on a TEM operating at an accelerating potential of 1 MeV, and show all atom positions across the boundary plane decisively resolved. At this operating voltage the instrumental resolution (Δx), given by

$$\Delta x = 0.6\, C_s^{1/4} \lambda^{3/4} \qquad (2)$$

is obviously dominated by the smaller electron wavelength, even with an accompanying order-of-magnitude increase in spherical aberration coefficient.[32] This is clearly the most desirable path of development for transmission electron microscopy, and holds the promise of routine atomic resolution images of grain boundaries in all classes of materials.

IV. SUMMARY

Although one of the earliest successes of the FIM was its clarification of the structure of high angle grain boundaries (viz., ruling out the "amorphous boundary layer" concept),[7] it has lost considerable ground to the TEM in more recent attempts at direct imaging of boundary structure. The limitations of the FIM in this regard are overwhelming: geometrical aberrations in the ion projection path, loss of detail in low index pole regions, fixed specimen orientation, and field induced distortions, including preferential evaporation at the boundary plane. Associated with this latter problem is the requirement that the specimen be able to sustain a high surface field in the first place. This immediately limits the possible range of FIM specimens to good electrical conductors, and even then many metals (e.g., Al, Mg, Zn, Ti) succumb to the high electrostatic forces on the emitter tip during operation.

As a consequence of these difficulties, grain boundary studies with the FIM have shifted emphasis away from structure towards composition. When interfaced with a time-of-flight mass spectrometer, the FIM-atom probe[33] has the potential for determining the precise concentration and distribution of segregate species at grain boundaries in candidate specimens.[34] Judging from the more recent reviews on the topic,[35] this type of application, coupled with TEM analysis, appears to be the most likely course of future development in field ion microscopy.

In extremely rapid parallel development, the resolution and stability refinements continually being incorporated in the conventional TEM have made possible the recent appearance of the atomic resolution microscope (ARM). With essentially no need for further enhancement, deconvolution, or processing, the photographs produced in the ARM give a direct visual representation of atomic structure as projected through the thickness of the specimen. Metals, semiconductors, insulators, and complex alloys are all amenable to study by this technique[36] and the first in-situ observation of atomic motion across a moving interface has already been reported.[37] Obviously, there is immeasurable benefit to be derived from the further development and immediate application of atomic resolution microscopy in grain boundary research.

ACKNOWLEDGEMENTS

The author would like to thank Prof. R.W. Balluffi for his invitation to present this review and Prof. R.J. Bayuzick for helpful direction on the topic of field ion microscopy.

This work was supported by the Division of Materials Sciences, Office of Basic Energy Sciences, U.S. Department of Energy under Contract No. W-7405-Eng-48.

REFERENCES

1. G.A. Chadwick and D.A. Smith (eds.), Grain Boundary Structure and Properties, Academic Press, London, 1976.
2. W. Bollmann, Crystal Defects and Crystalline Interfaces, Springer-Verlag, New York, NY, 1970.
3. W. Gaudig and S.L. Sass, Phil. Mag. 39A, 725 (1979).
4. M.P. Seah, Surf. Sci. 53, 168 (1975).
5. D.R. Clarke, in Proc. 37th Ann. EMSA, G.W. Bailey (ed.), Claitor's, Baton Rouge, LA, 1979, p. 486.
6. E.W. Müller, Adv. Electronics and Electron Physics, 13, 83 (1960).
7. E.W. Müller and T.T. Tsong, Field Ion Microscopy, Principles and Applications, American Elsevier, NY, 1969.
8. K.M. Bowkett and D.A. Smith, Field Ion Microscopy, North Holland, Amsterdam, 1970.
9. E.W. Müller, J. Appl. Phys. 27, 474 (1956).
10. S.S. Brenner, in High Temperature, High Resolution Metallography, H.I. Aaronson and G.S. Ansell (eds.), Gordon and Breach, NY, 1967, p. 281.
11. H.N. Southworth and J.M. Walls, Surf. Sci. 75, 129 (1978).
12. D.G. Brandon, J. Sci. Inst. 41, 373 (1964).
13. H.C. Tong and J. Washburn, Crystal Lattice Defects 2, 221 (1971).
14. K.D. Rendulic and E.W. Müller, J. Appl. Phys. 38, 2070 (1967).

15. E.W. Müller in Modern Diffraction and Imaging Techniques in Materials Science, S. Amelinckx, R. Gevers, G. Remaut and J. Van Landuyt (eds.), North-Holland, Amsterdam, 1970, p. 711.

16. E.W. Müller, Surf. Sci. 2, 484 (1964).

17. B. Ralph, Surf. Sci. 23, 130 (1970).

18. R.J. Bayuzick and R.S. Goodrich, Surf. Sci. 23, 225 (1970).

19. P.L. Bolin, R.J. Bayuzick and B.N. Ranganathan, Phil. Mag. 32, 891 (1975).

20. D.A. Smith and G.D.W. Smith in Proc. 3rd Int. Conf. on the Strength of Metals and Alloys, Cambridge, England, Vol. I, 1973, p. 144.

21. P.B. Hirsch, A. Howie, R.B. Nicholson, D.W. Pashley and M.J. Whelan, Electron Microscopy of Thin Crystals, Krieger, NY, 1977.

22. J.W. Edington, Practical Electron Microscopy in Materials Science, Monographs 1-5, Macmillan/Philips Technical Library, Eindhoven, 1974-1977.

23. G. Thomas and M.J. Goringe, Transmission Electron Microscopy of Materials, J. Wiley-Interscience, NY, 1979.

24. M. Born and E. Wolf, Principles of Optics, 5th ed., Pergamon, Oxford, 1975.

25. J.M. Cowley, Diffraction Physics, North Holland, Amsterdam, 1975.

26. D.L. Misell, J. Phys. A 6, 62 (1973).

27. O. Scherzer, J. Appl. Phys. 20, 20 (1949).

28. R. Sinclair, R. Gronsky and G. Thomas, Acta Met. 24. 789 (1976).

29. K. Izui, S. Furano and H. Otsu, Jap. J. Electron Micros. 26, 129 (1977).

30. R. Gronsky and G. Thomas, Scripta Met. 11, 791 (1977).

31. O.L. Krivanek, S. Isoda and K. Kobayashi, Phil. Mag. 36, 931 (1977).

32. H. Ichinose, Y. Ishida and M. Mori, in Proc. Ninth Int. Cong. Elec. Microsc., Vol. I, J.M. Sturgess (ed.), Imperial Press, Ontario, 1978, p. 413.

33. E.W. Müller, J.A. Panitz and S.B. McLane, Rev. Sci. Inst. 39, 83 (1968).

34. P.J. Turner and J.M. Papazian, Metal Sci. J. 1, 82 (1973).

35. P.H. Cutler and T.T. Tsong (eds.), Field Emission and Related Topics, North Holland, Amsterdam, 1978, published as Surface Science 70 (1978).

36. R. Gronsky, D.R. Clarke and G. Thomas, in Electron and Positron Spectroscopies in Materials Science and Engineering, O. Buck (ed.), Academic Press, NY, 1979, p. 275.

37. H. Hashimoto, Y. Takai, Y. Yokota, A. Kumao, H. Endoh, E. Fukuda and H. Tomioka, in Proc. 37th Ann. EMSA, G.W. Bailey (ed.), Claitor's, Baton Rouge, LA, 1979, p. 384.

FIGURE CAPTIONS

Fig. 1 Schematic illustration of the atomic arrangement in an FIM emitter tip. Note that the density of protruding surface atoms (S) is greater near high-index plane surfaces (viz., H) than at low-index plane surfaces (viz., L).

Fig. 2 Schematic illustration showing the actual trajectory (dashed line) of an ion striking the screen at X' and the points predicted by various standard geometrical projections (G,S,B, and O; see text for details) from the same object point, X.

Fig. 3 (a) FIM micrograph of a fully ordered Ni_4W specimen and (b), its corresponding stereographic projection (courtesy of Tong and Washburn, ref. 13).

Fig. 4 Computer simulated FIM image of an f.c.c. crystal in an [001] zone orientation (courtesy of J. Washburn).

Fig. 5 Schematic illustration showing grain boundary contrast in an FIM image. Atomic level detail at (a) is likely to be distorted due to off-axis projection and at (b), appears only within one of the contiguous grains.

Fig. 6 (a) FIM micrograph of antiparallel twin boundary (A-A) in ordered Ni_4W, and (b) corresponding stereographic projection. Note that where the boundary passes the congruent plane $(12\bar{1})//(121)$ and $(2\bar{1}\bar{1})//(\bar{2}11)$, ring mismatch disappears (coutesy of Tong and Washburn, ref. 13).

Fig. 7 FIM image of an iridium specimen showing a grain boundary node made up of three small angle grain boundaries, all related by rotations about an axis near to the [100] tip direction, after B. Ralph, ref. 17.

Fig. 8 FIM micrograph of a high angle grain boundary in tungsten, marked by inked-in white spots. The misorientation is 64° about [110] (from Bayuzick and Goodrich, ref. 18).

Fig. 9 FIM micrograph of tungsten equilibrated in a low pressure of oxygen, showing bright spots at the grain boundary (arrowed) associated with oxygen segregation, after Smith and Smith, ref. 20.

Fig. 10 Comparison of the optical ray diagram and mathematical description of the image formation process for transmission electron microscopy.

Fig. 11 Computed phase contrast transfer functions 2 sin $X(\underset{\sim}{q})$ for 100 kV electrons and C_s = 0.7 mm. Defocus values are (a) 0, (b) -600, (c) -1200, and (d) -1400Å respectively.

Fig. 12 Optical diffractograms from TEM images at (a) "exact" focus, (b) -800Å defocus and (c) -2200Å defocus. The diffuse halo representing the main transfer interval extends radially outward with underfocus, causing an increase in image contrast (note increase in diffraction spot intensity from (a) to (c)), and resolution (new, higher order spots in (c)).

Fig. 13 Atomic resolution image of [110] oriented silicon, showing exact agreement with the projected atomic structure (one unit cell shown) even at 1.4Å interatomic separation, after Izui, et. al., ref. 29.

Fig. 14 Schematic electron diffraction pattern of a grain boundary. For the transfer limit shown by dashed lines, all of the low index planes in grain 1 will be imaged, denoting atom positions by their intersection. However, only a single set of low index planes from grain 2 will appear and atomic level detail is therefore lost.

Fig. 15 Photogram of a 3 mm diameter electron microscope support grid, used in the optical simulation experiments of Fig. 16. The specimen in this case possesses a central boundary between regions of wide and narrow grid spacings.

Fig. 16 Optical reconstruction of the "specimen" in Fig. 15, showing (a) an accurate image using full reconstruction; (b) loss of detail using high order truncation; (c) disappearance of boundary using identical first order reflections and (d) retrieval of boundary using different first order reflections. Details are explained in text.

Fig. 17 Lattice image, formed by combining the forward-scattered beam with one Bragg-scattered beam from each grain, of a small angle boundary in an Al-Zn alloy. Regions of local mismatch accommodation are arrowed.

Fig. 18 Lattice image of the same alloy as Fig. 17, but showing the close-packed planes which parallel the boundary plane. Arrowed microledges are a single interplanar spacing in height.

Fig. 19 Structural image of a small angle grain boundary in silicon formed by combining all of the first order reflections within a [$\bar{1}$10] zone.

Fig. 20 (a) Structural image of a high angle grain boundary in Ge (misorientation 39° about [011]) using all reflections out to 0.35$\mathring{A}^{-1}$, theextent of the first transfer interval). The detailed model of the atomic arrangements (b) resolve every atom across the boundary plane and no dangling bonds are observed (courtesy of O.L. Krivanek, ref. 31).

Fig. 21 Atomic resolution image of twin band in a gold foil for [110] oriented crystal; twin planes are arrowed (courtesy Y. Ishida, ref. 32).

Fig. 22 Atomic resolution image of a $\Sigma = 11$ CSL boundary in gold. Lattice point fitting reveals that mismatch is accommodated within the spacing of several {311} planes adjacent to the boundary, and no coincidence sites are actually observed at the boundary. Foil orientation is [110] (courtesy of Y. Ishida, ref. 32).

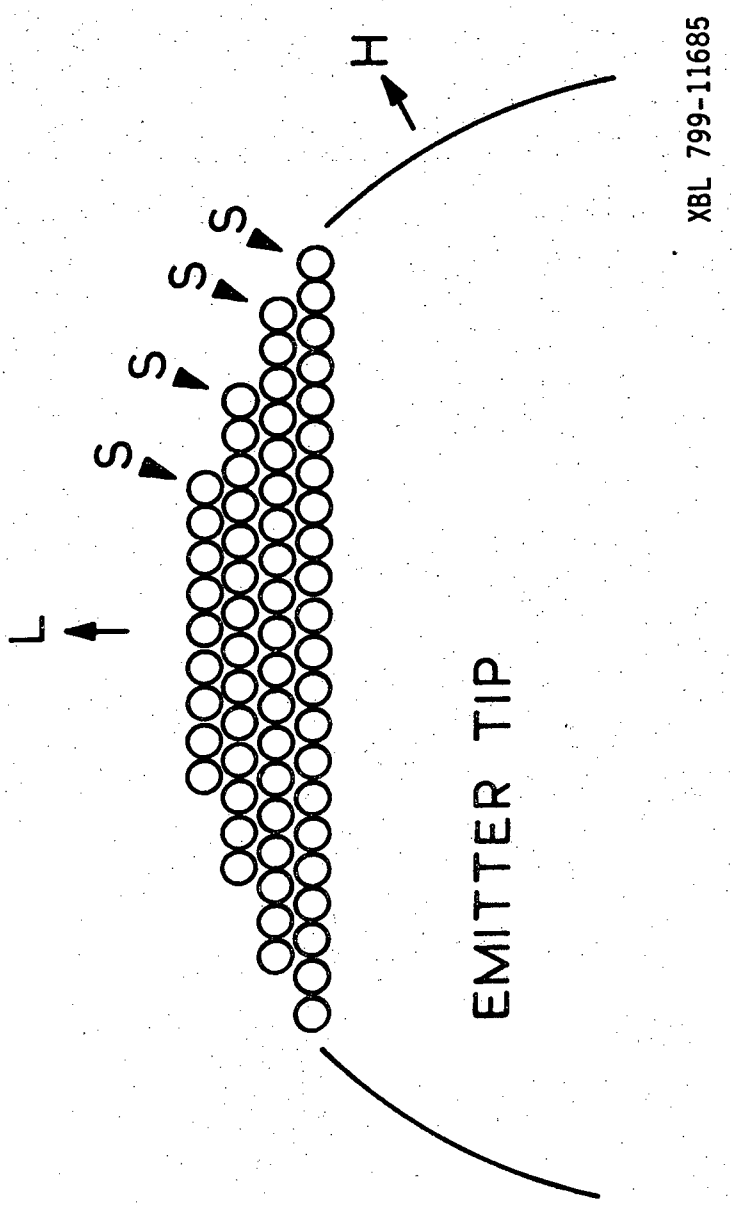

Fig. 1

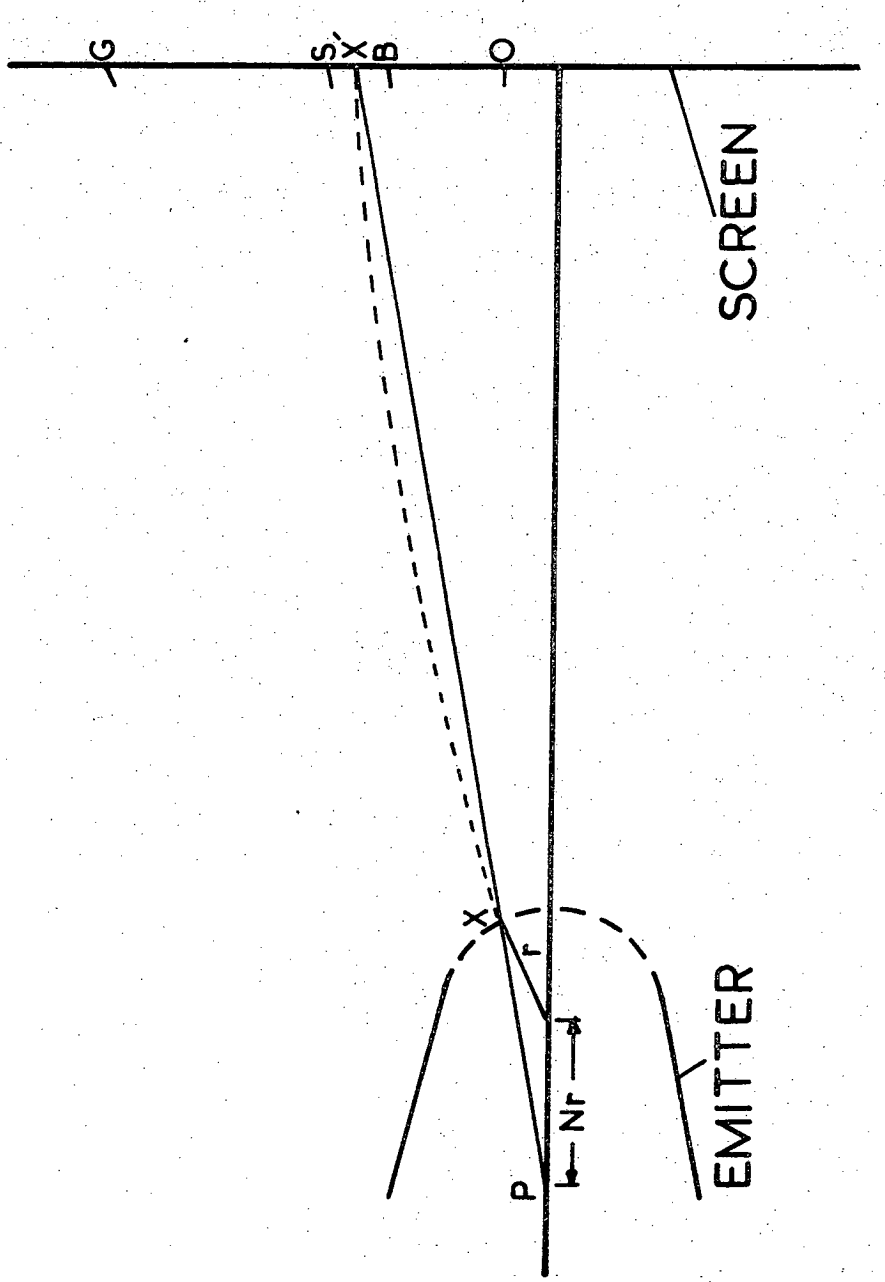

XBL 799-11683

Fig. 2

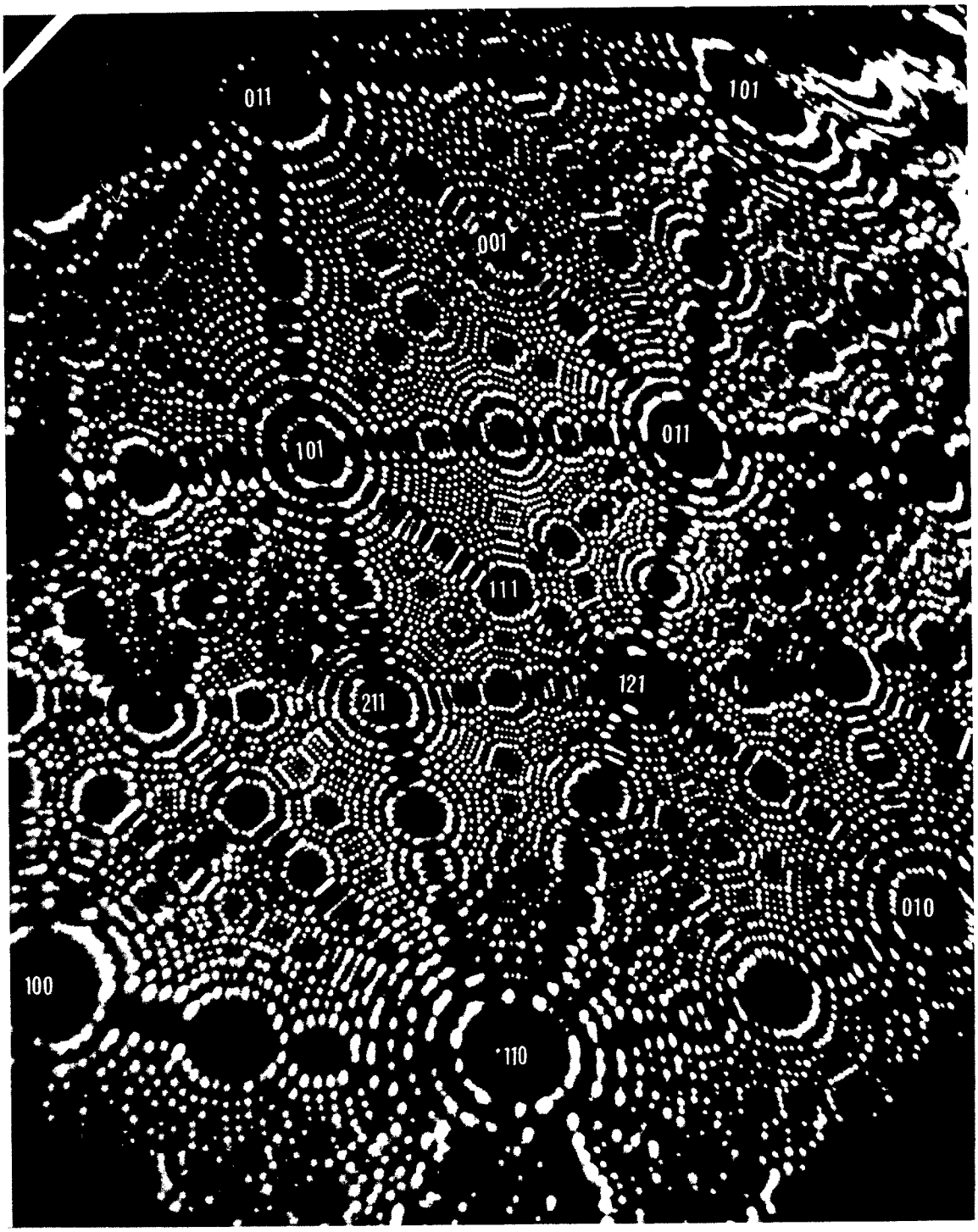

XBB 715 1883

Fig. 3(a)

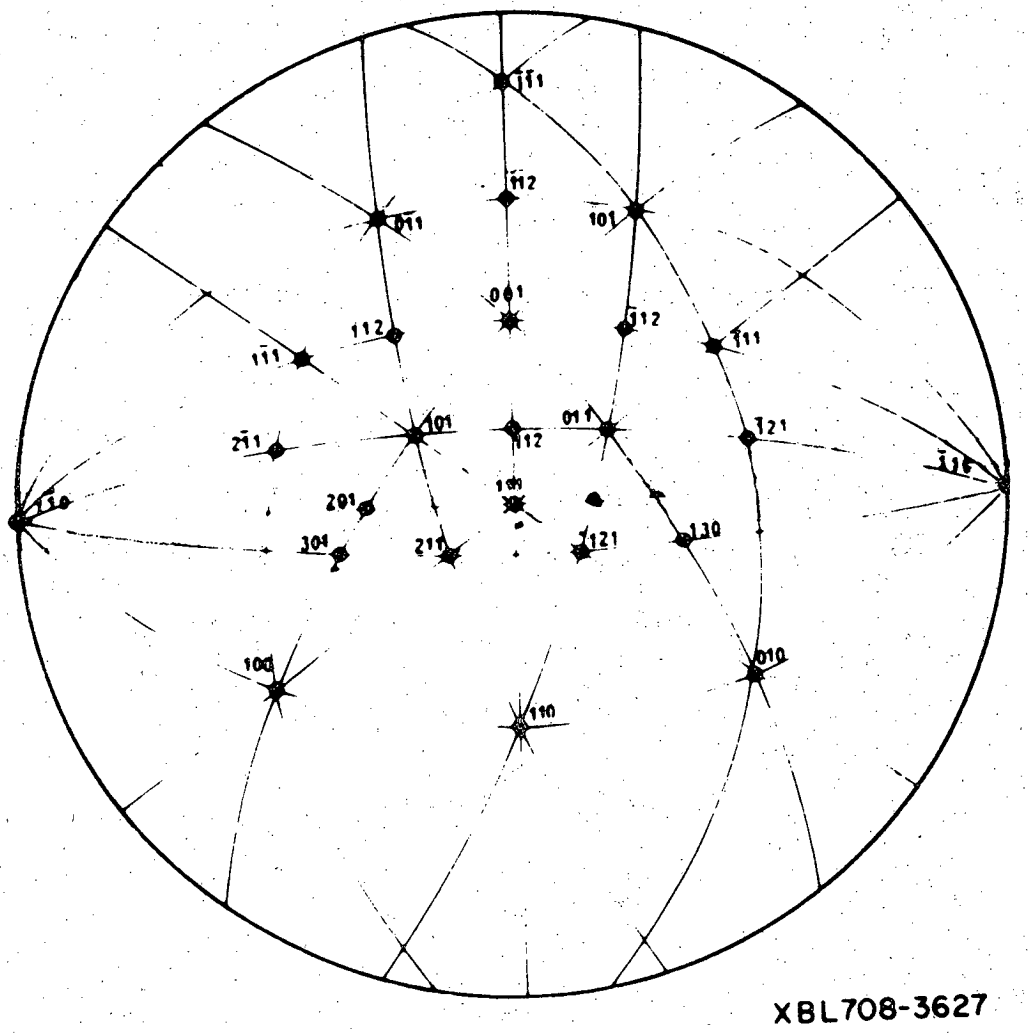

Fig. 3(b)

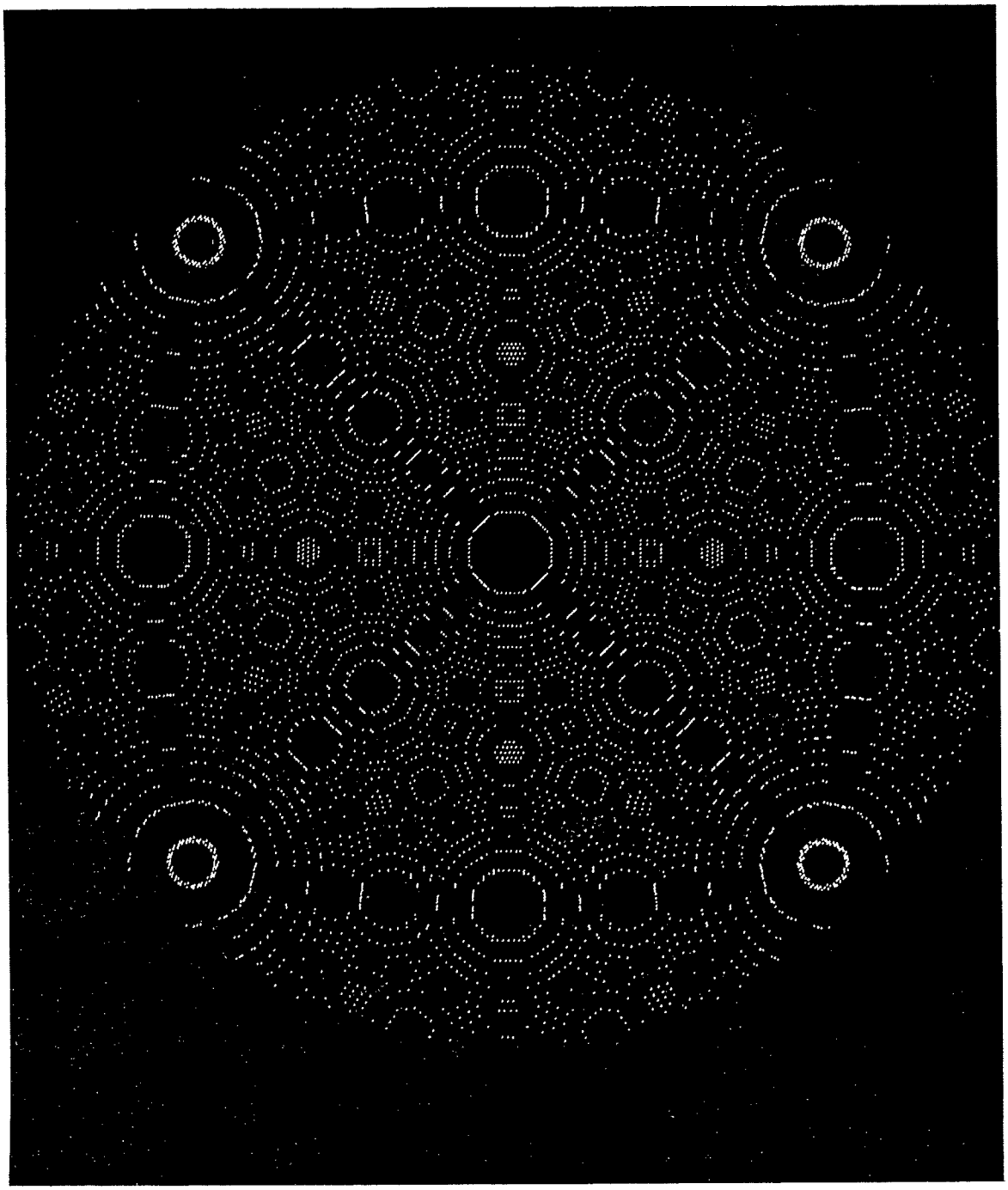

XBB 715 1888

Fig. 4

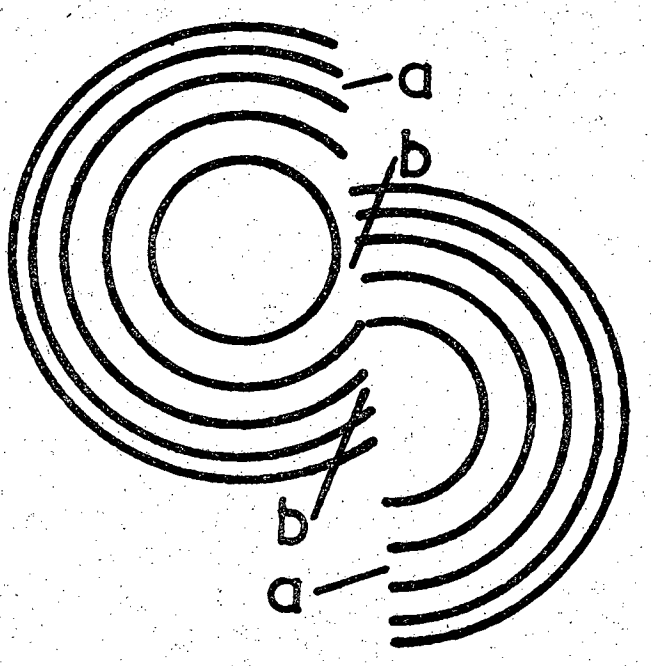

XBL 799-11684

Fig. 5

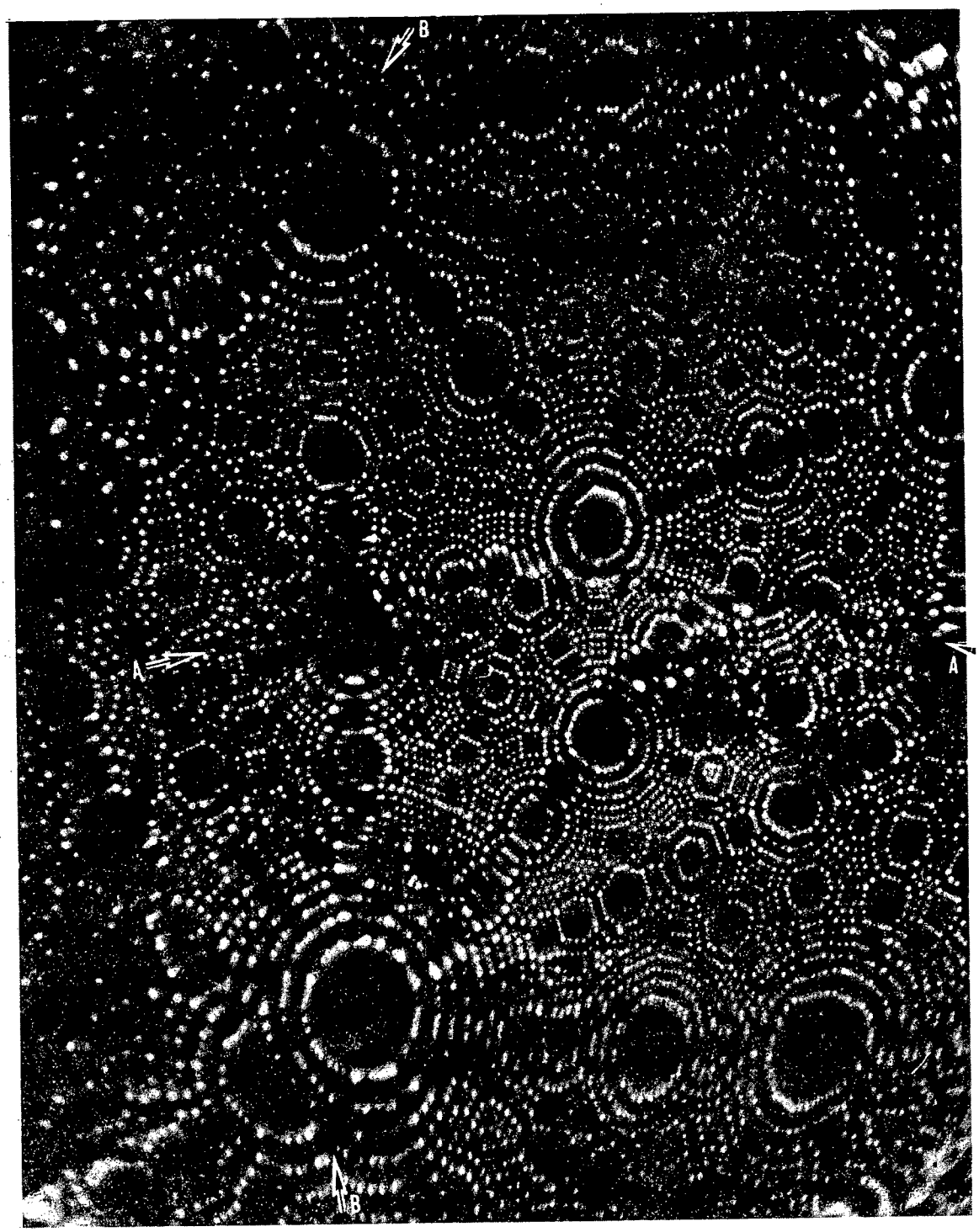

XBB 715 1884

Fig. 6(a)

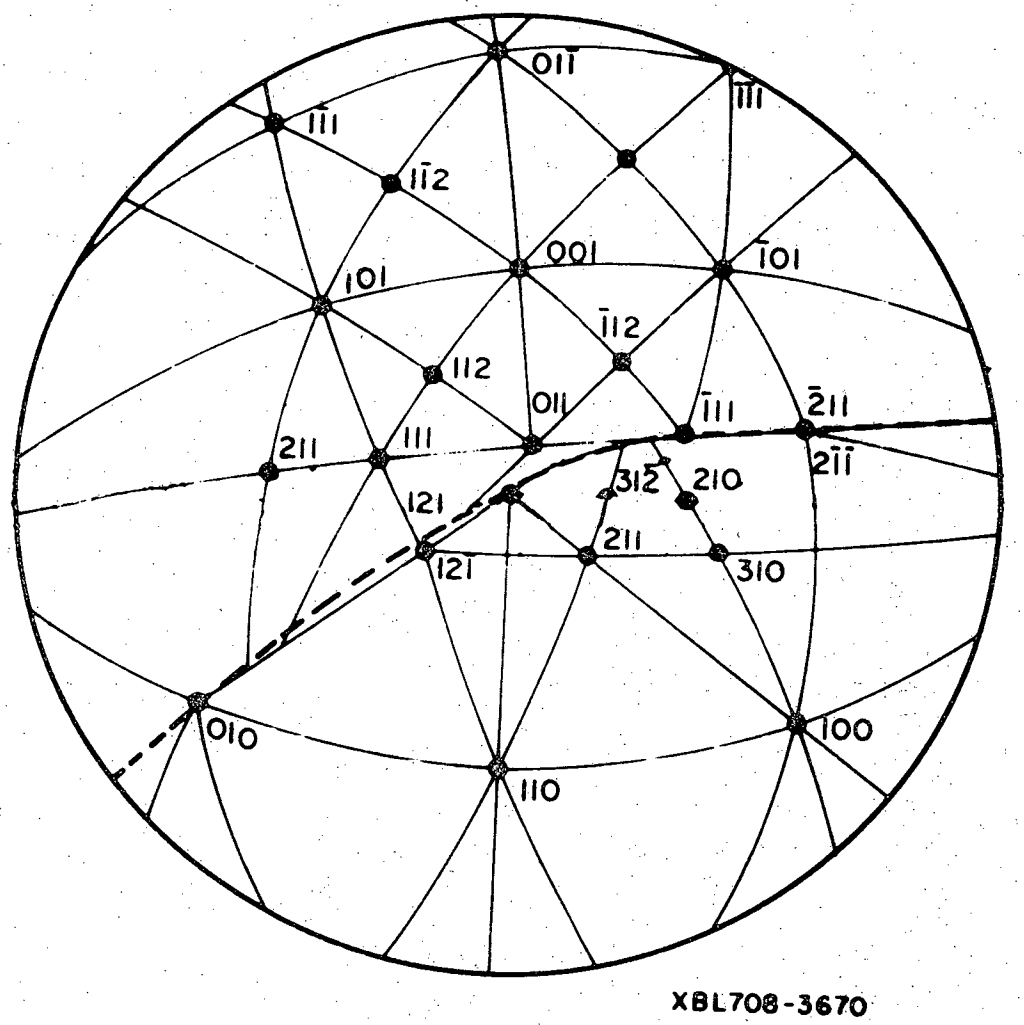

XBL708-3670

Fig. 6(b)

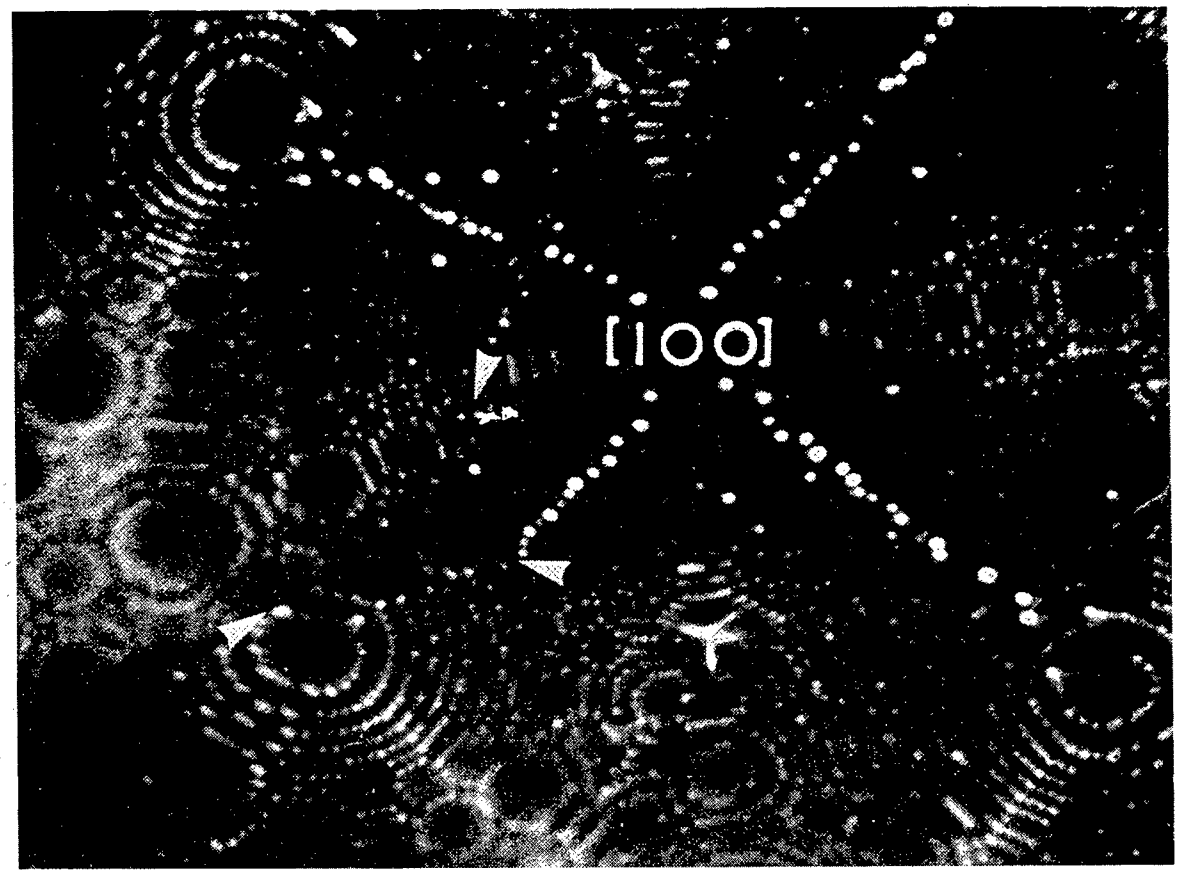

XBB 799 11493

Fig. 7

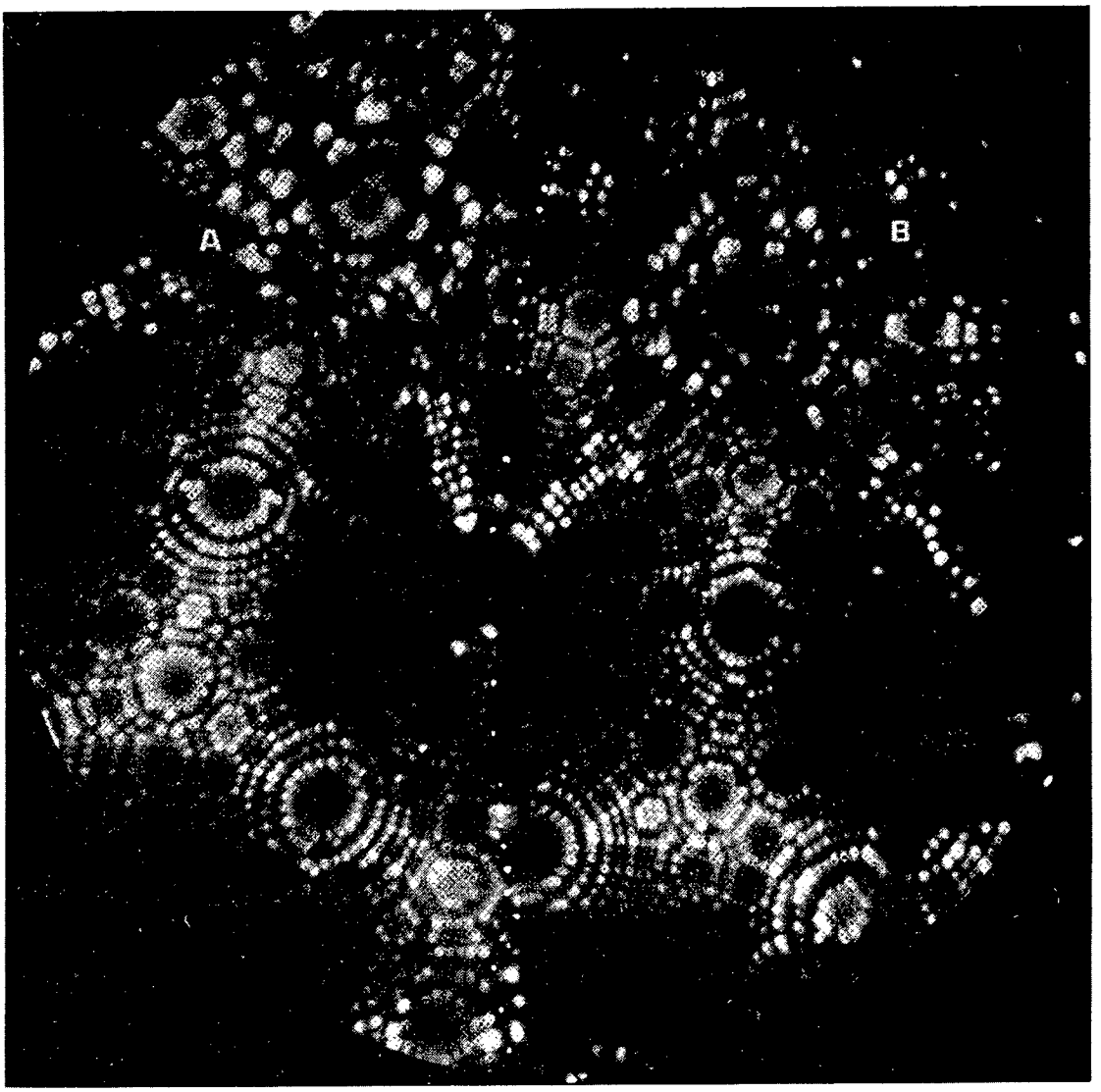

XBB 799 11492

Fig. 8

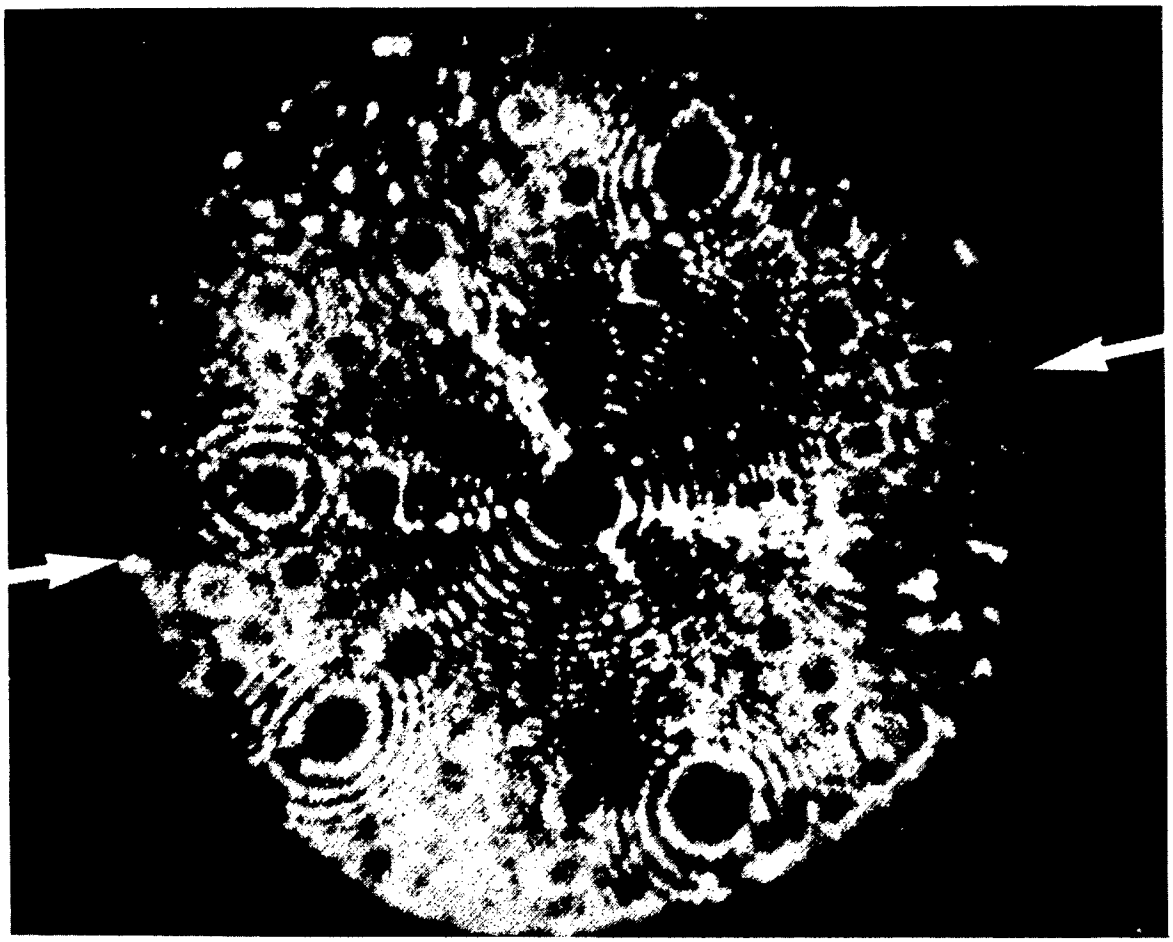

XBB 799 11490

Fig. 9

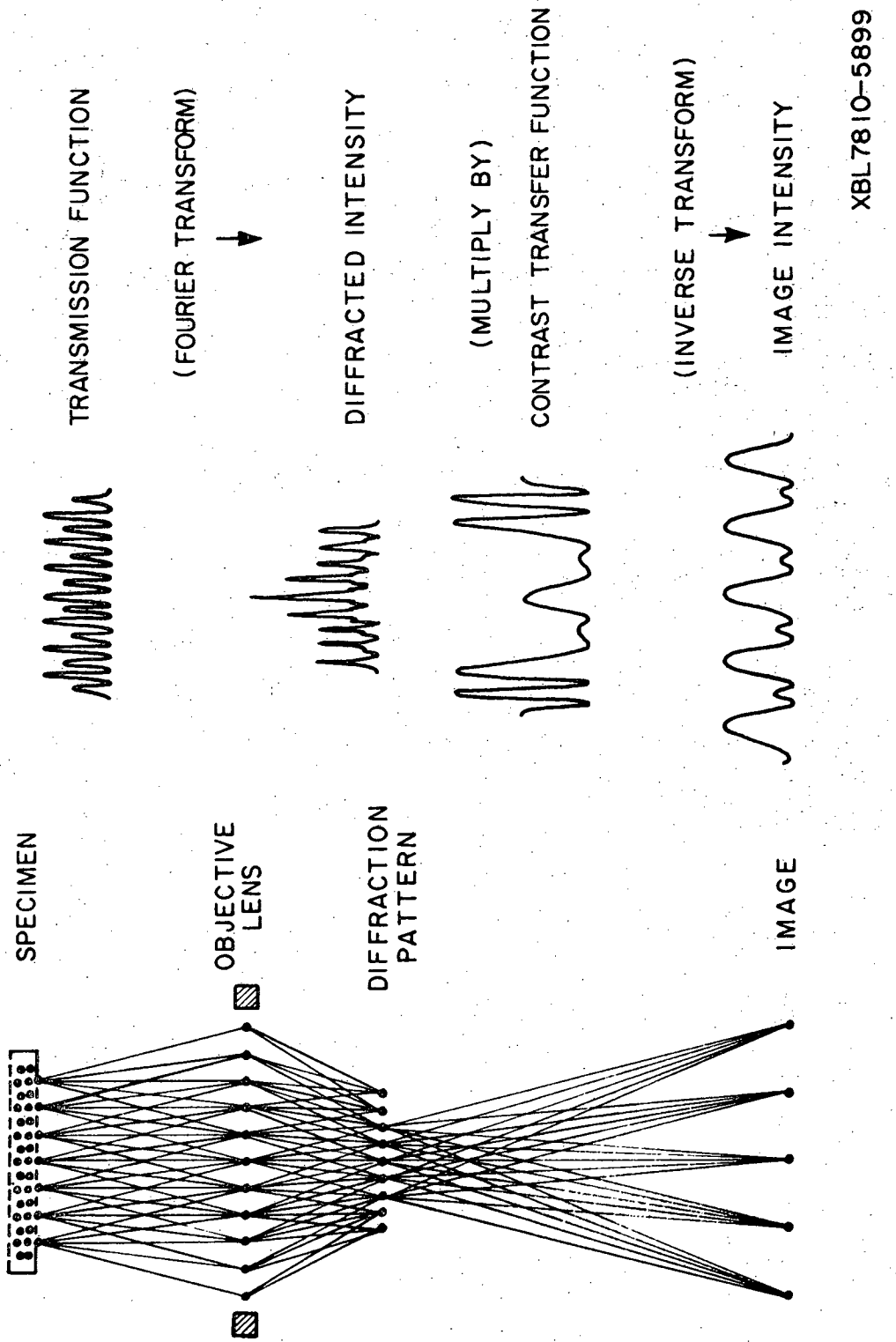
SPECIMEN
OBJECTIVE LENS
DIFFRACTION PATTERN
IMAGE
TRANSMISSION FUNCTION
(FOURIER TRANSFORM)
DIFFRACTED INTENSITY
(MULTIPLY BY)
CONTRAST TRANSFER FUNCTION
(INVERSE TRANSFORM)
IMAGE INTENSITY
XBL7810-5899

Fig. 10

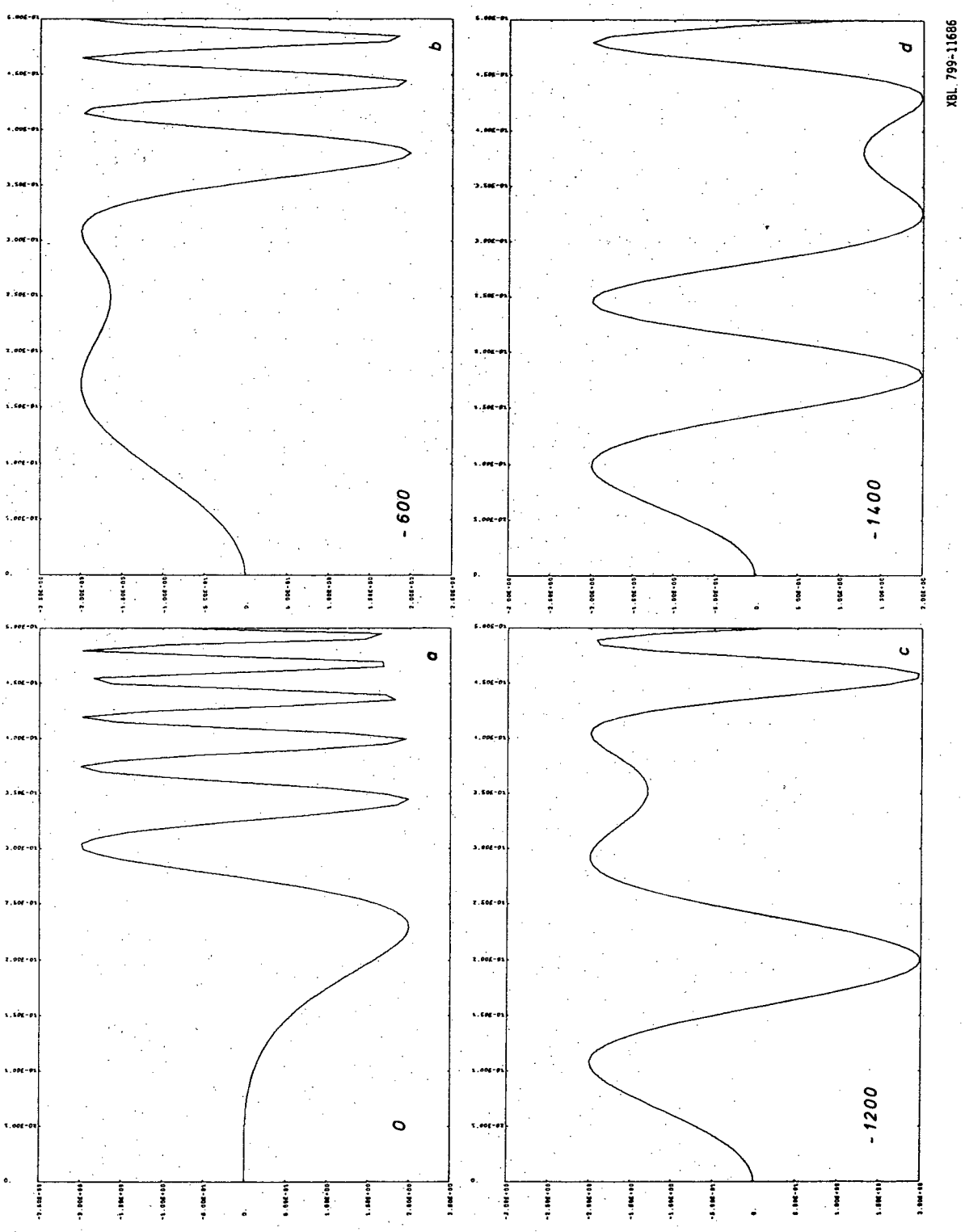

XBL 799-11686

Fig. 11

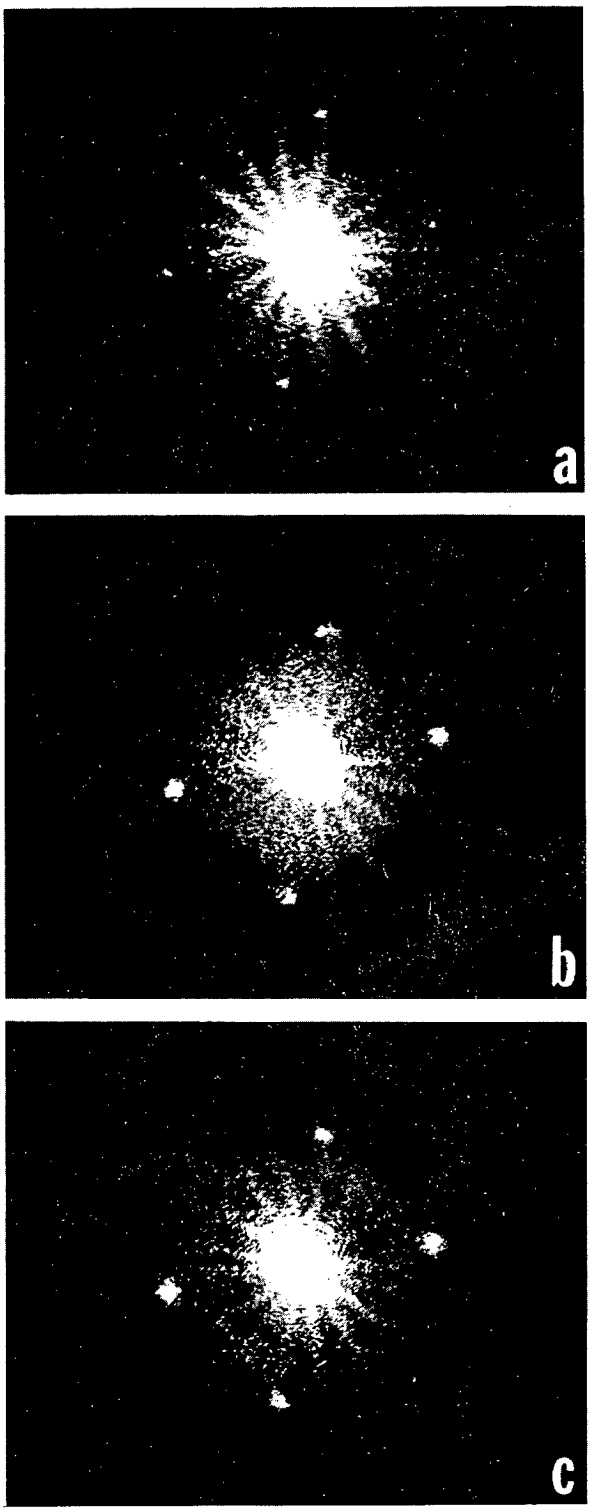

XBB 795 7080

Fig. 12

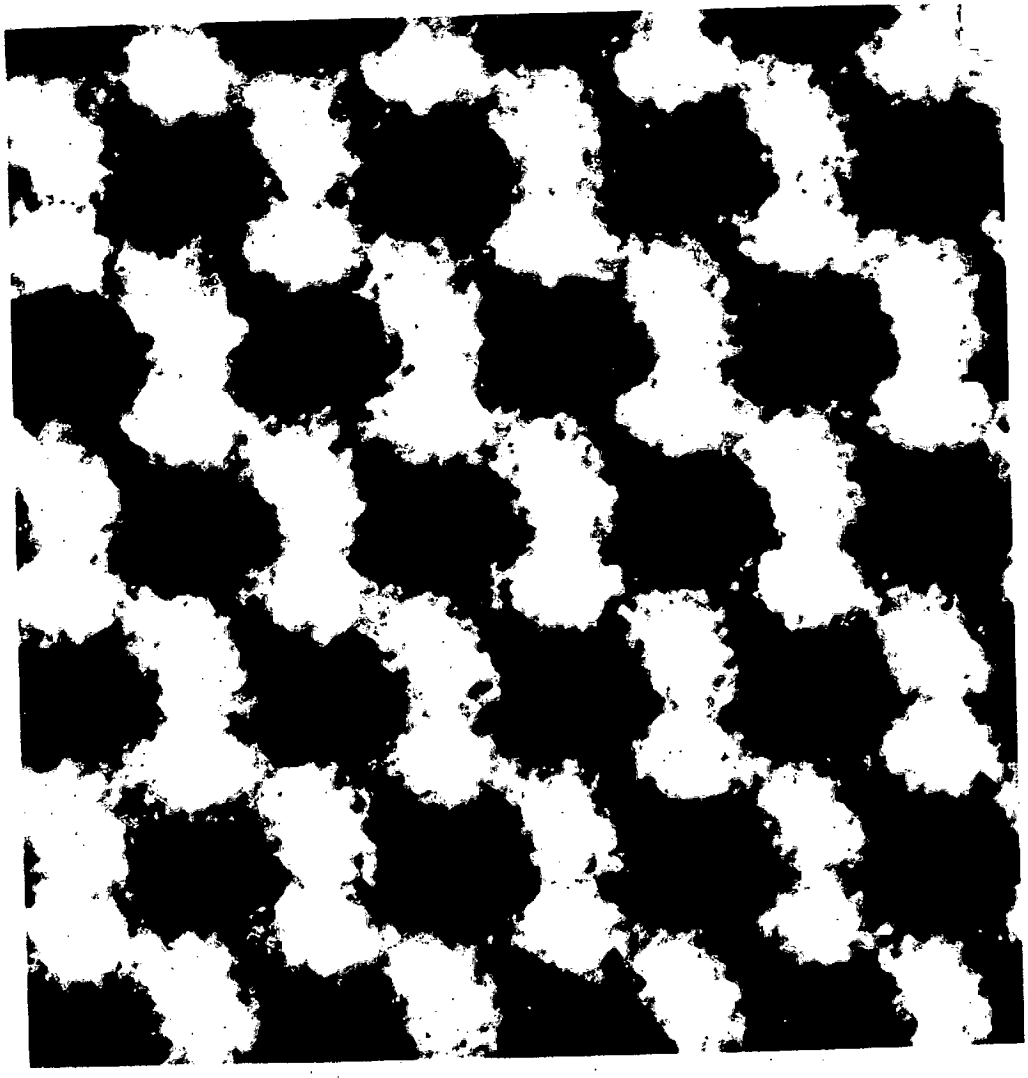

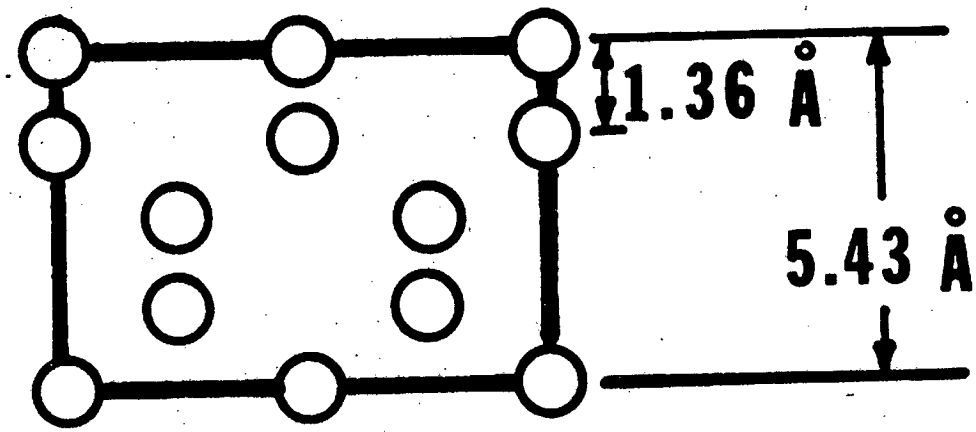

XBB 780 15547

Fig. 13

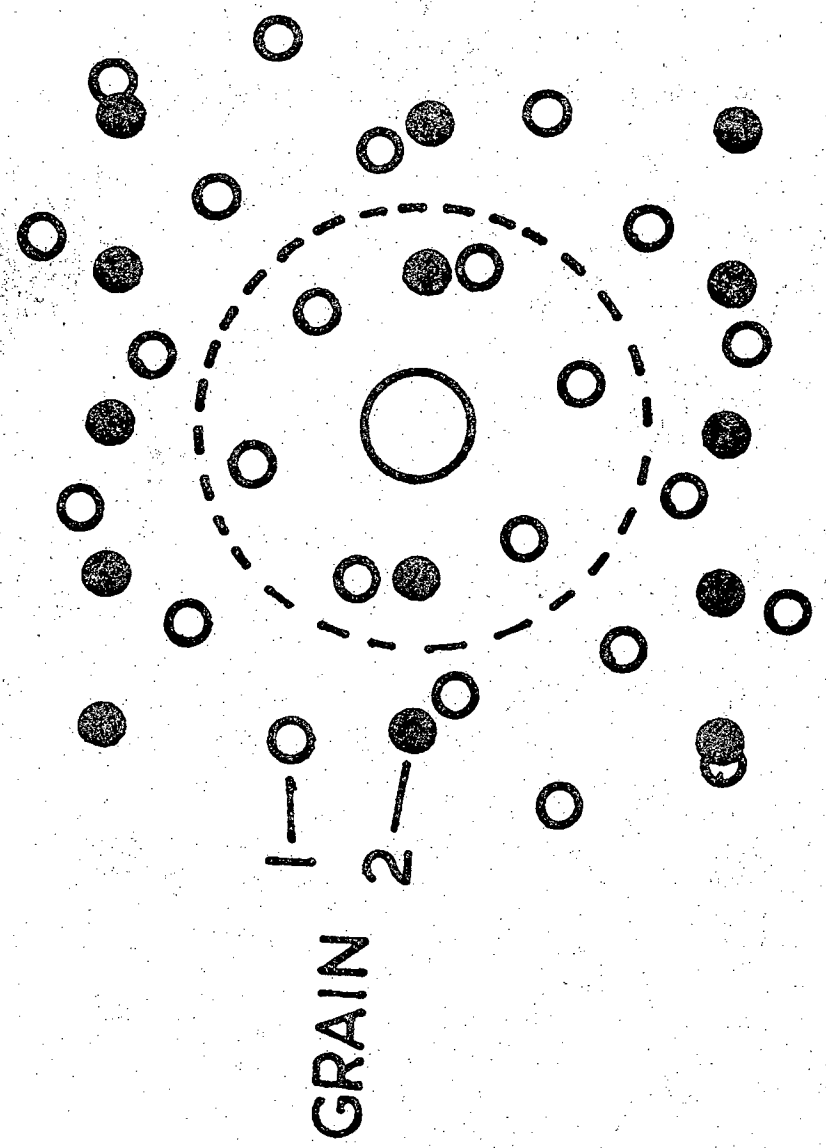

XBL 799-11682

Fig. 14

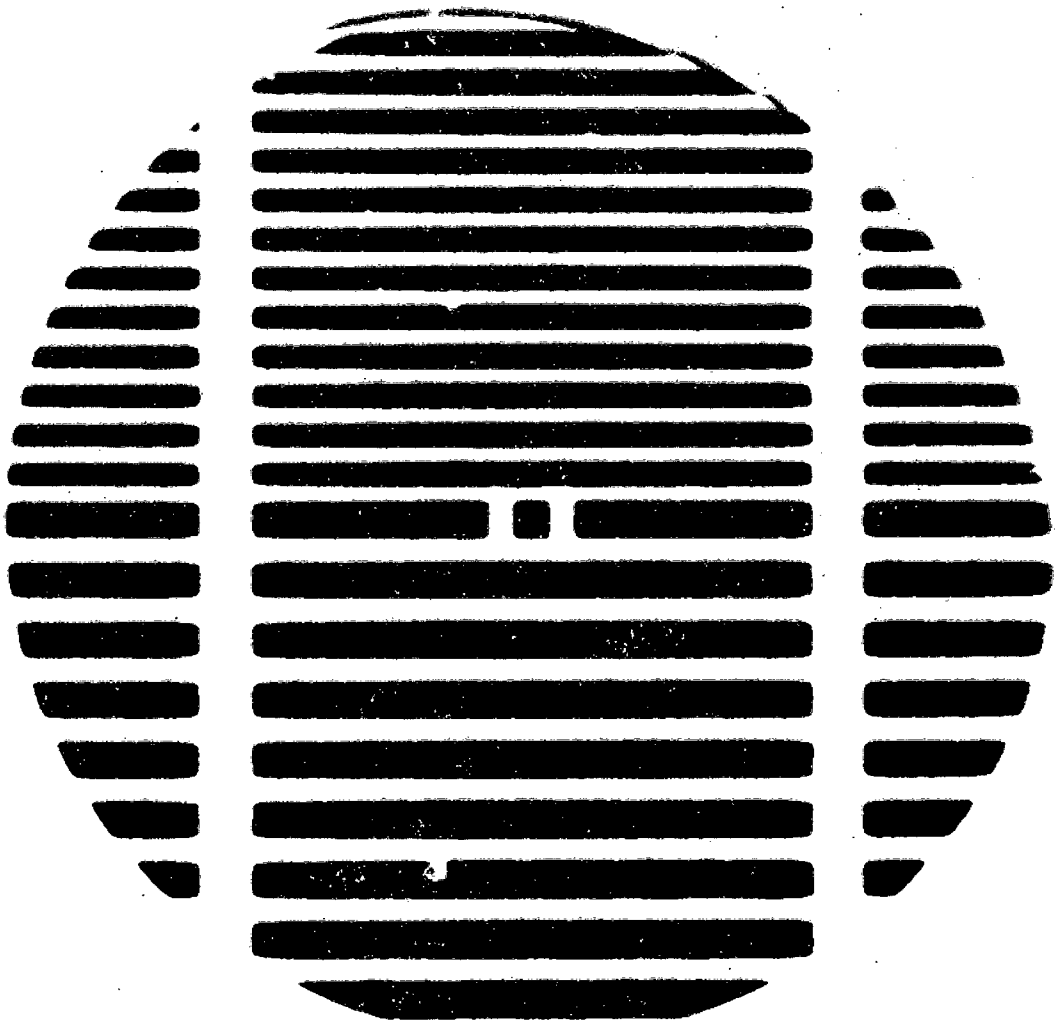

XBB 798 10349

Fig. 15

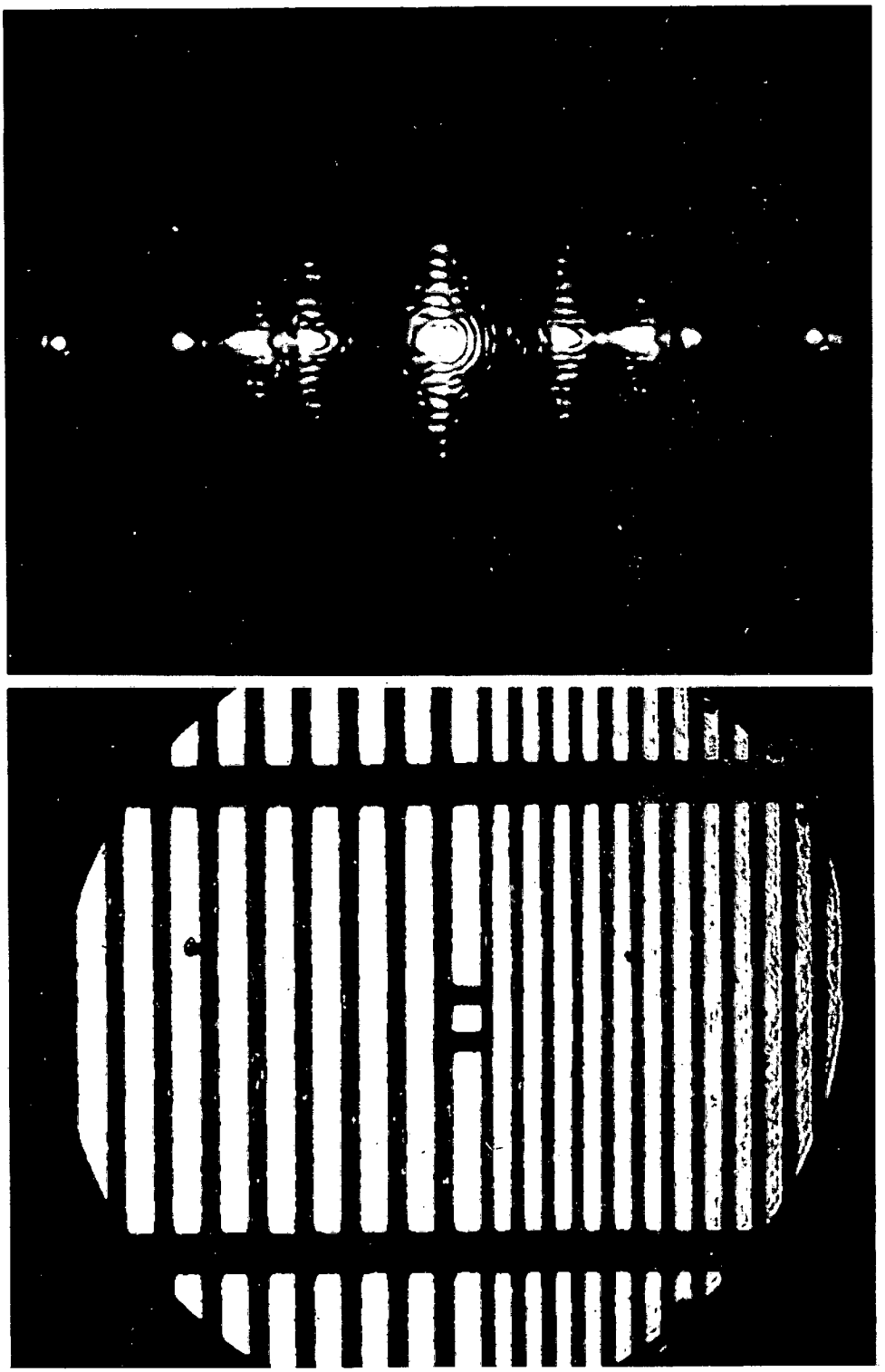

XBB 798 10348

Fig. 16(a)

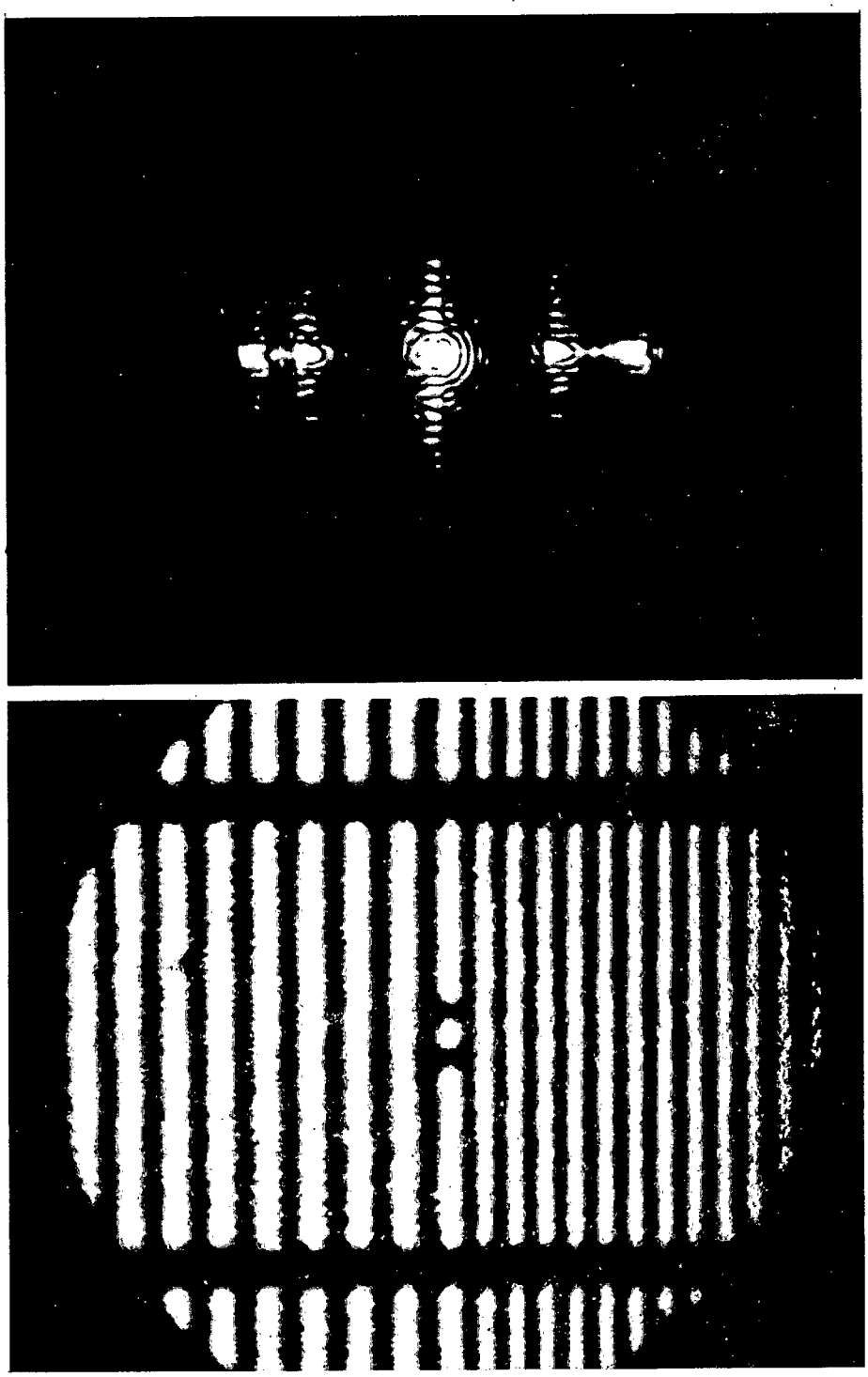

XBB 798 10347

Fig. 16(b)

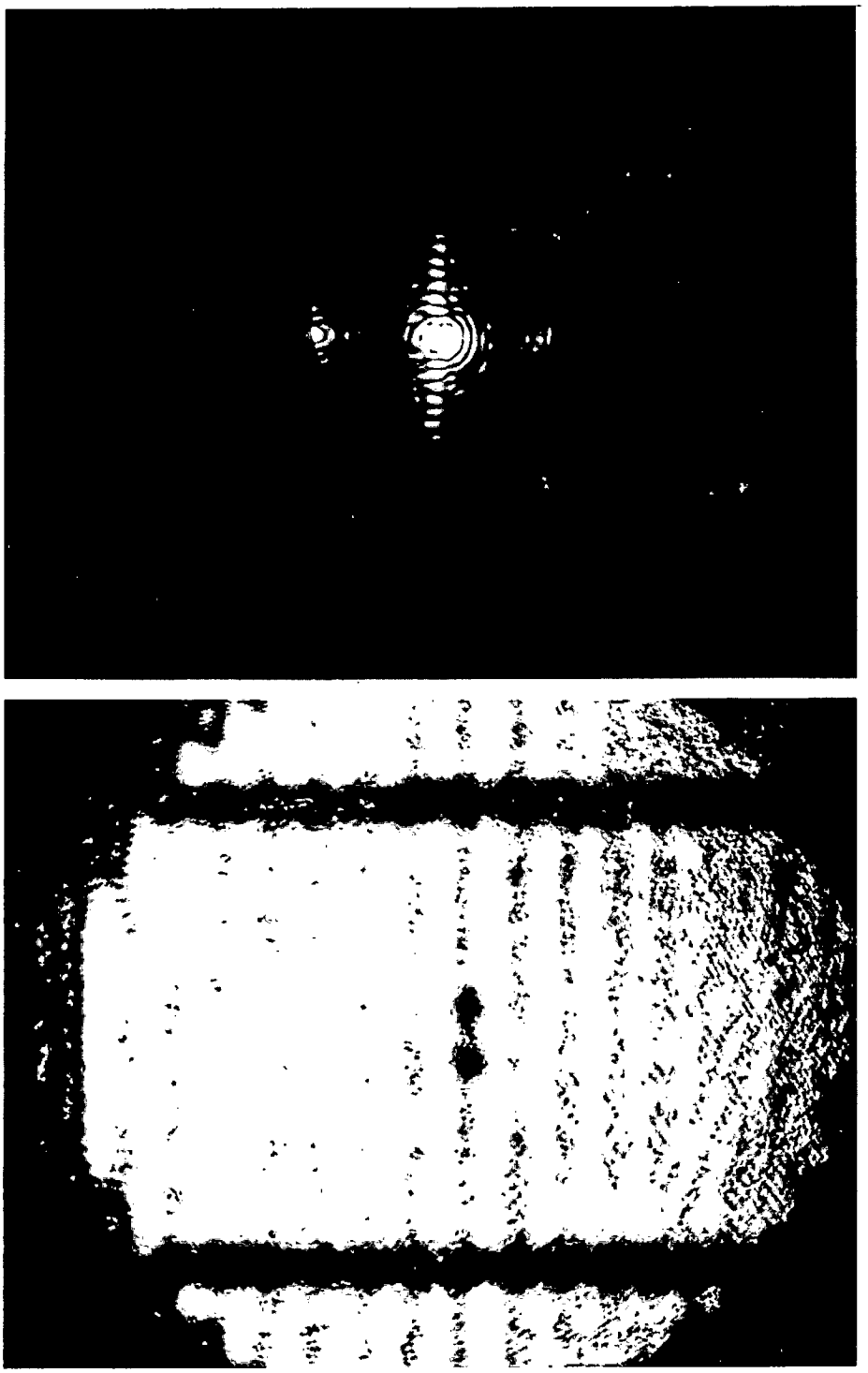

XBB 798 10346

Fig. 16(c)

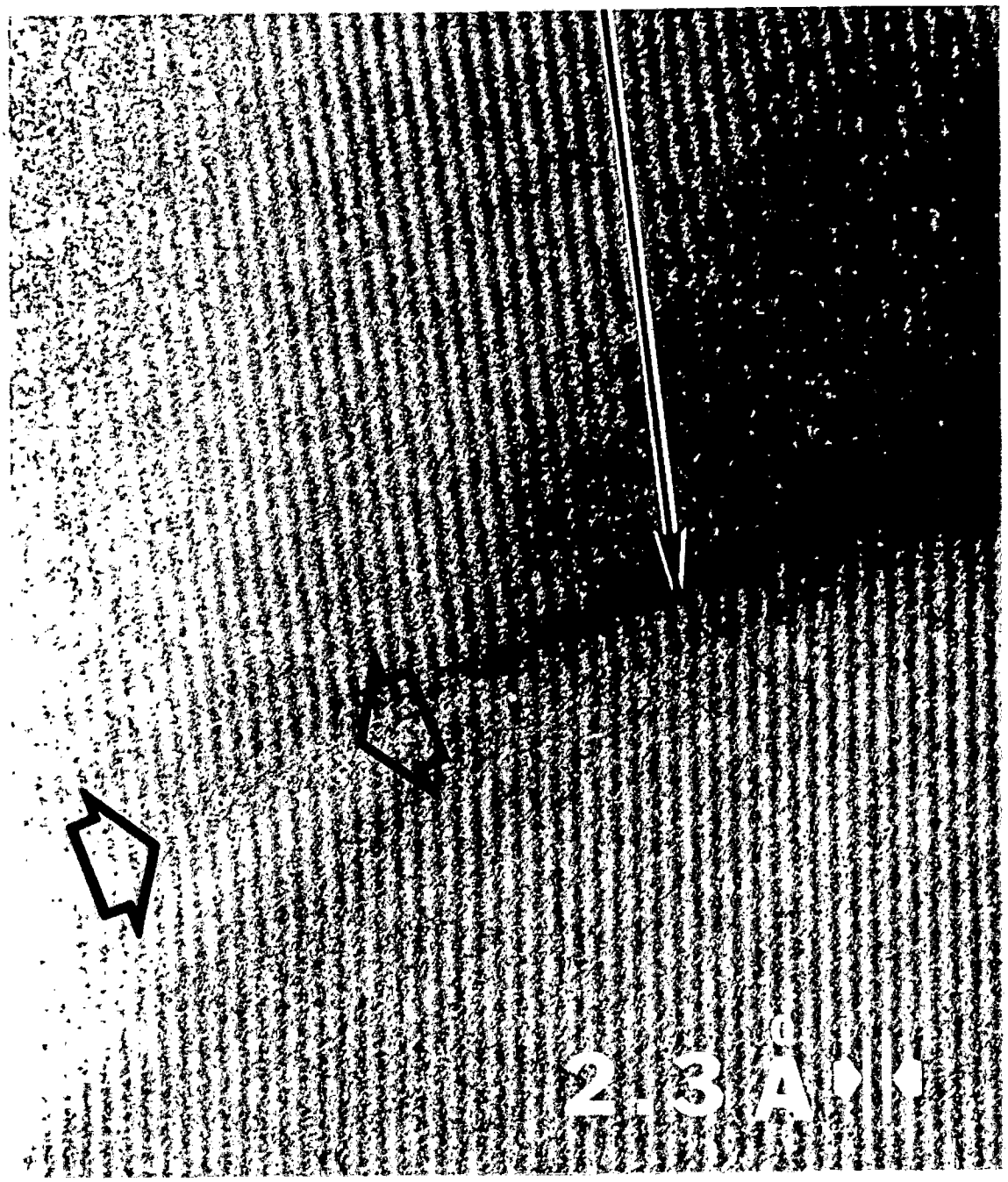

XBB 760 10531

Fig. 17

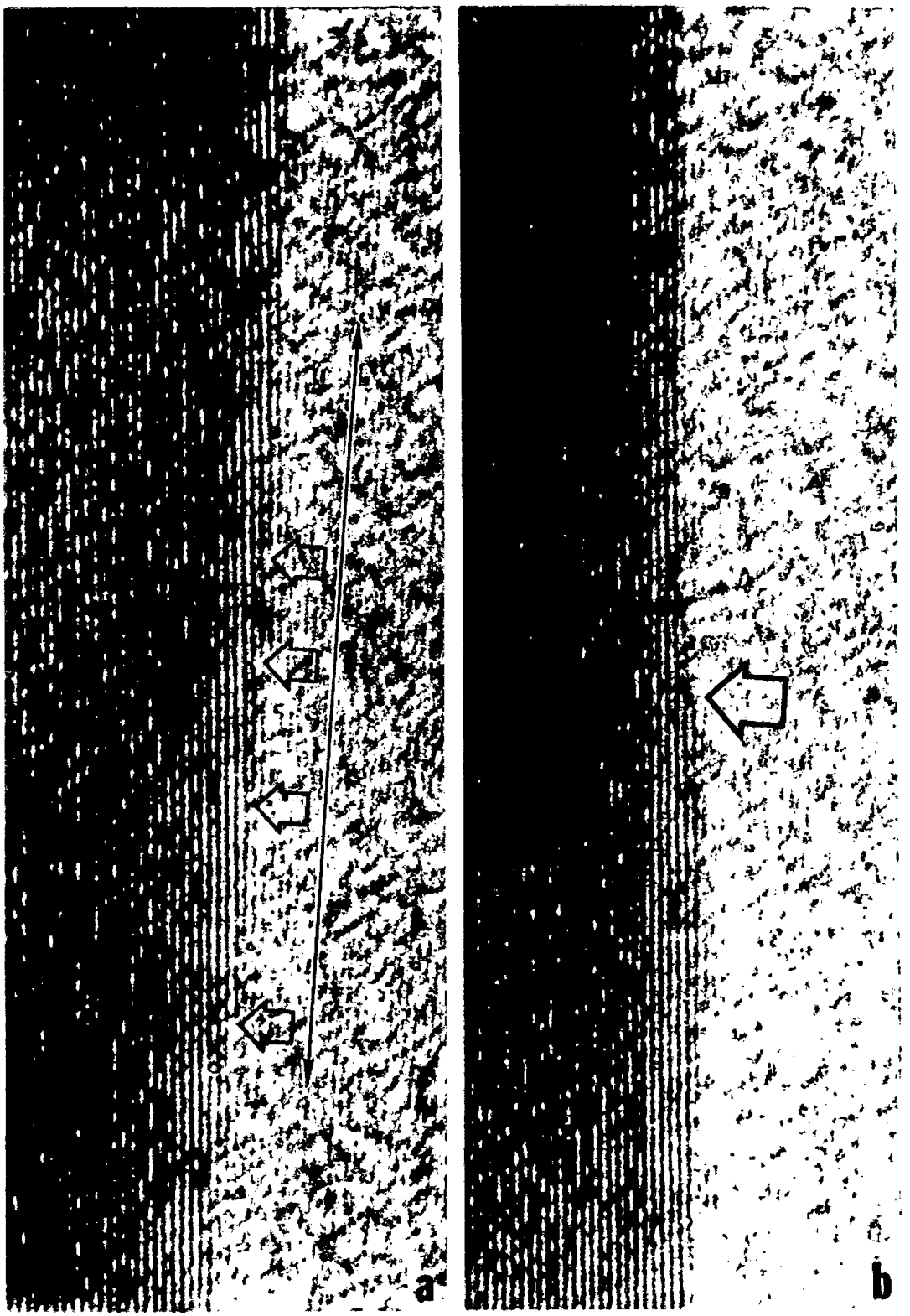

XBB 760 10511

Fig. 18

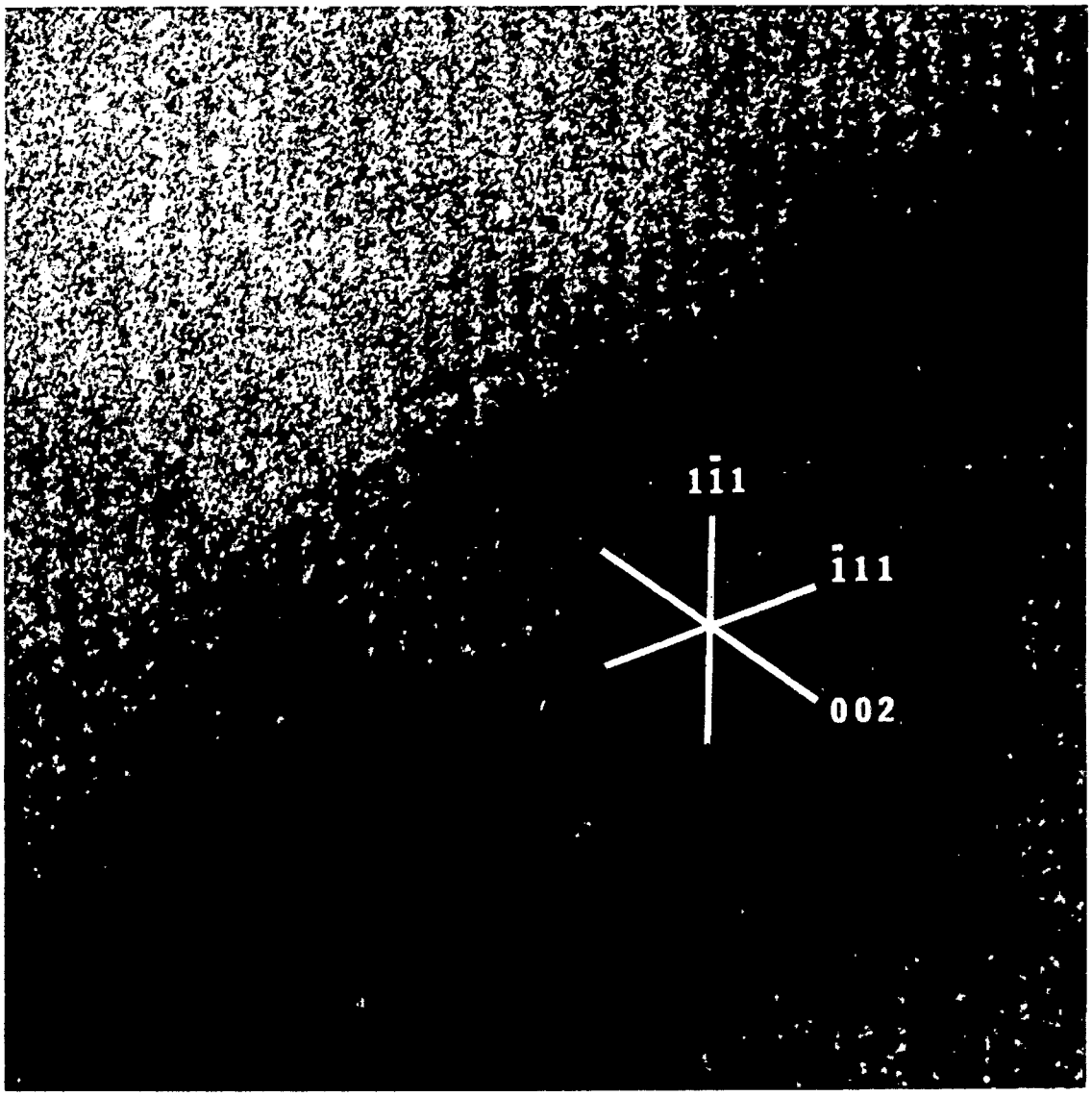

XBB 795 7087

Fig. 19

XBB 774 2837

Fig. 20(a)

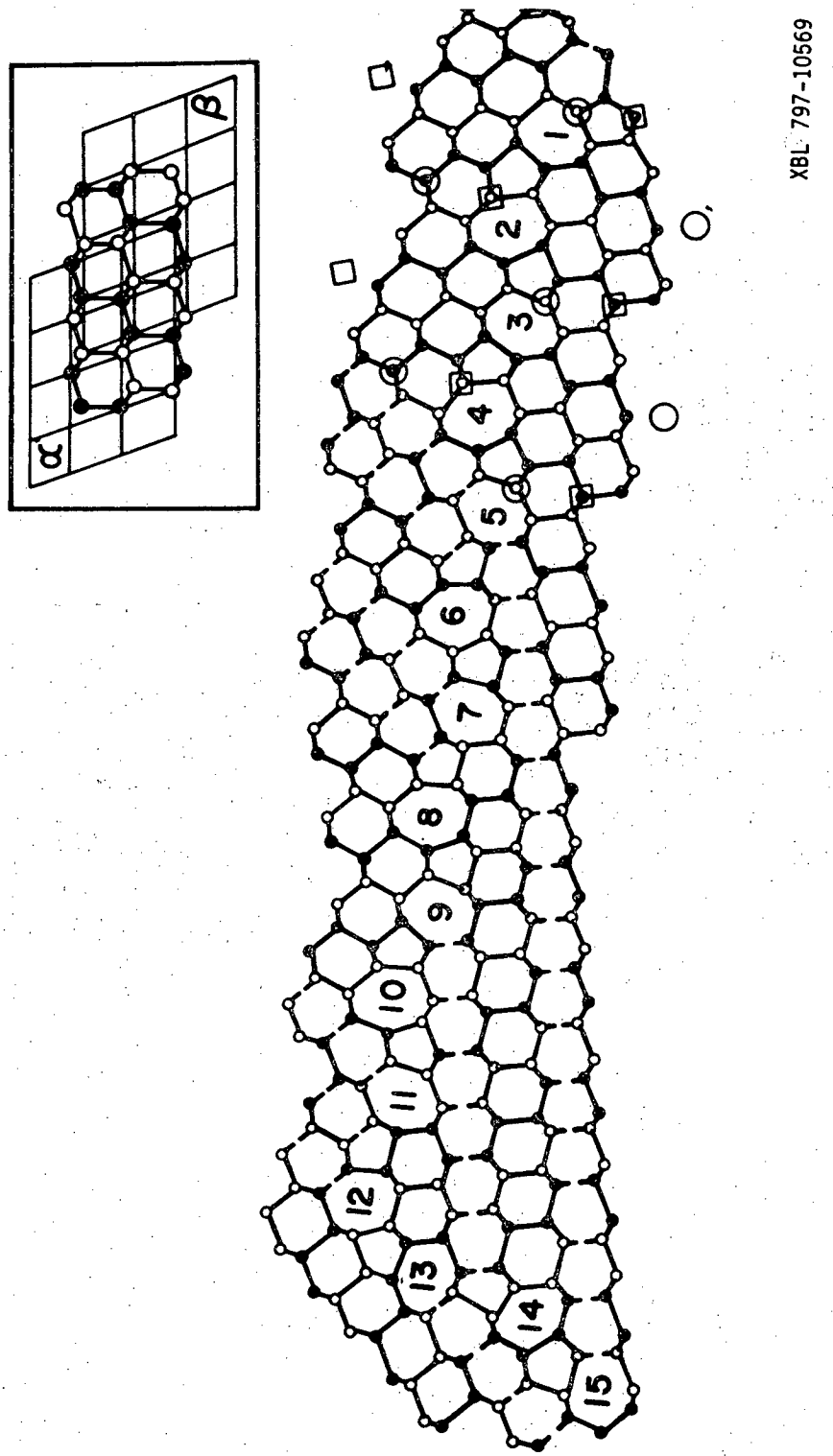

Fig. 20(b)

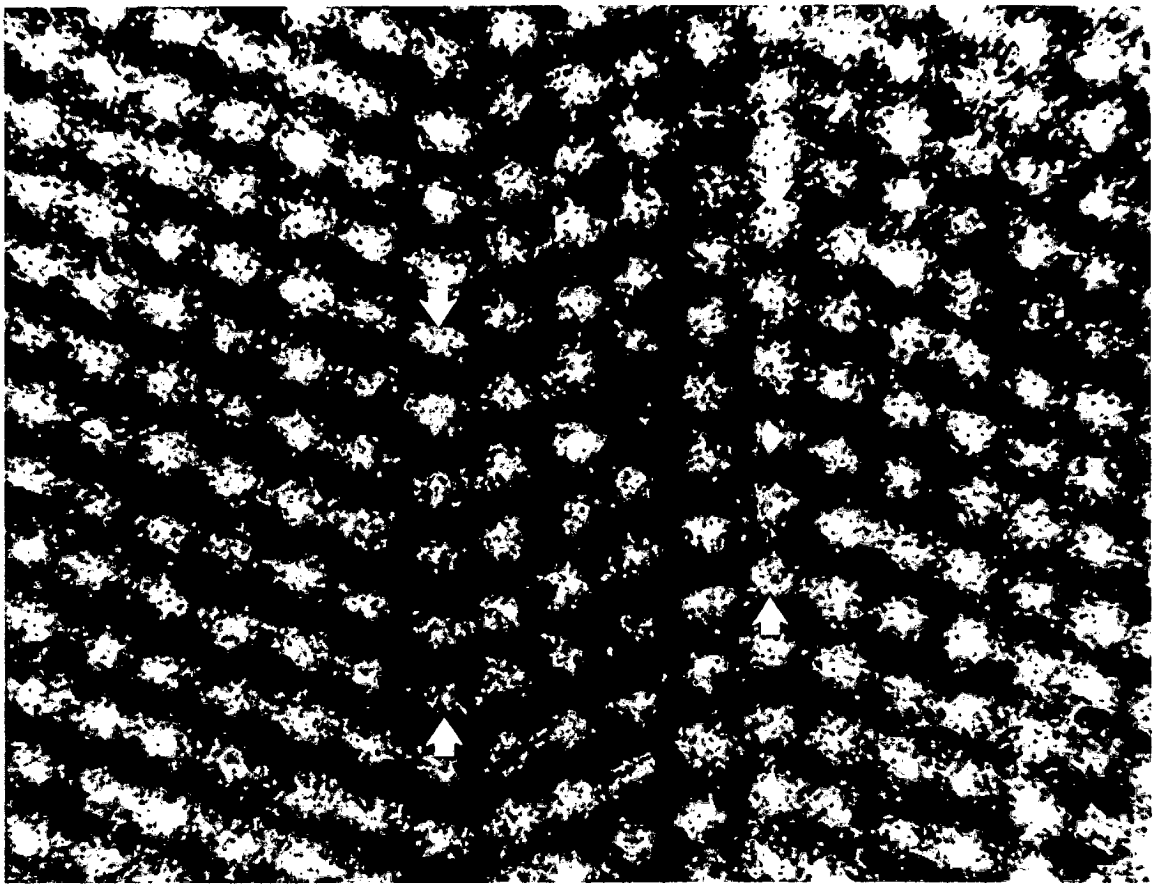

XBB 795 7081

Fig. 21

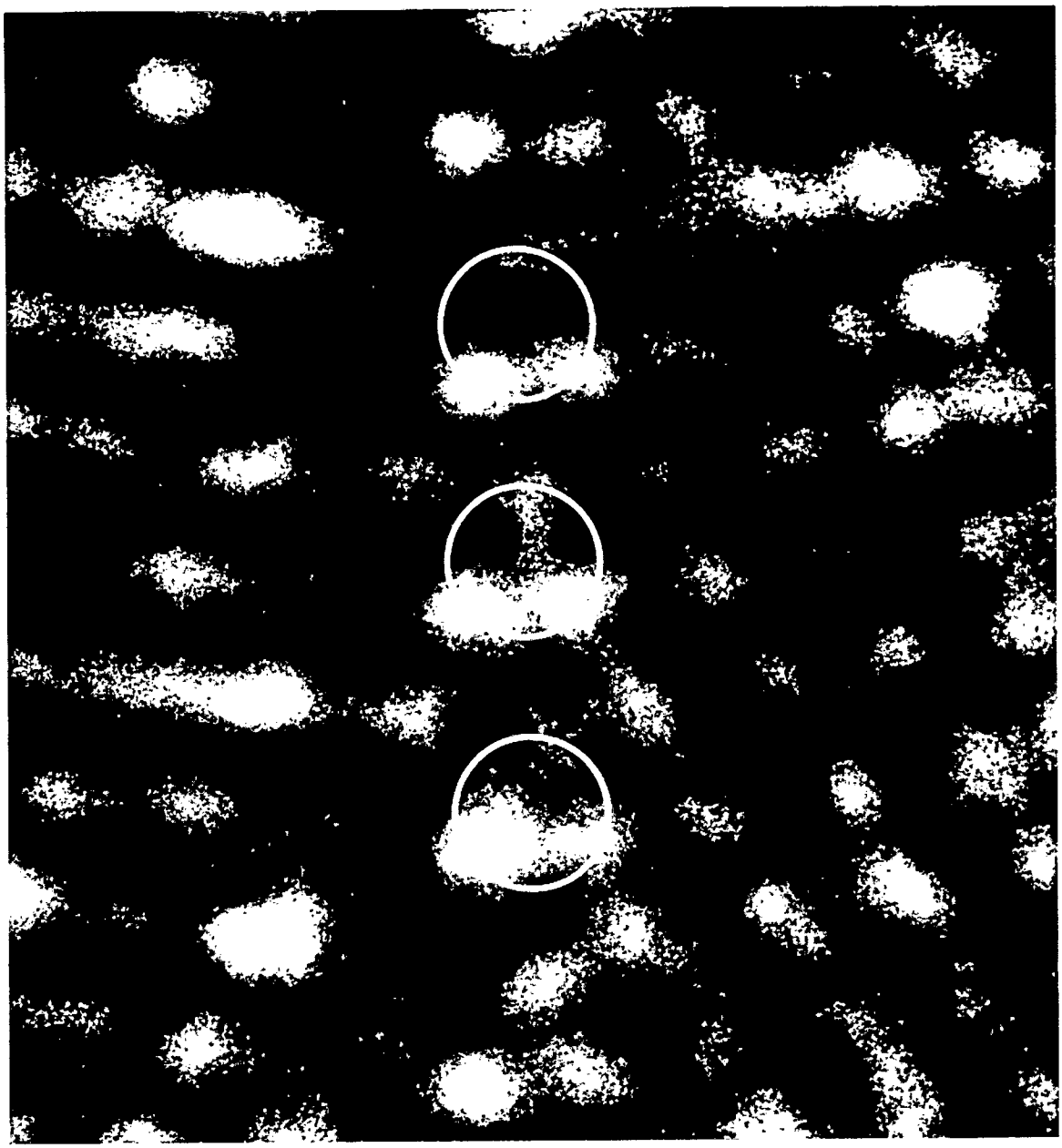

XBB 795 7082

Fig. 22

This report was done with support from the Department of Energy. Any conclusions or opinions expressed in this report represent solely those of the author(s) and not necessarily those of The Regents of the University of California, the Lawrence Berkeley Laboratory or the Department of Energy.

Reference to a company or product name does not imply approval or recommendation of the product by the University of California or the U.S. Department of Energy to the exclusion of others that may be suitable.

TECHNICAL INFORMATION DEPARTMENT
LAWRENCE BERKELEY LABORATORY
UNIVERSITY OF CALIFORNIA
BERKELEY, CALIFORNIA 94720